Accommodation of plate motion in an incipient strike-slip system: the Central Walker Lane

Enter authors here: Ian K.D. Pierce [1], Steven G. Wesnousky [1], Lewis A. Owen [2], Xinnan Li[3], and Marc Caffee[4]

[1.] Center for Neotectonic Studies and Seismological Laboratory, University of Nevada, Reno, NV 89557, USA

[2.] Department of Geology, University of Cincinnati, Cincinnati, OH 45221, USA

[3.] Institute of Geology, China Earthquake Administration, Beijing, China 100029

[4.] PRIME Lab, Purdue University, West Lafayette, IN 47907, USA

Corresponding author: Ian K.D. Pierce (ian@nevada.unr.edu)

Key Points:

- Slip rates of normal faulting for the Antelope, Smith, and Mason valley rangefront faults are 0.6 $^{+0.7}/_{-0.3}$, 0.7 $^{+1.0}/_{-0.4}$, and <0.05 mm/yr, respectively.
- Shear in the western Central Walker Lane is accommodated along a system of short, left-stepping en-echelon dextral and normal faults.
- Some geodetic shear remains unaccounted for by geologic rates, but is likely accommodated by off-fault deformation and complex rupture patterns.

Abstract

Geodetic studies in the Central Walker Lane report that ~7–8 mm/yr of right-lateral shear is accumulating across the region. The rates and patterns of active faults bounding and within the Walker Lake basin and Antelope, Smith, and Mason valleys in the western part of the Central Walker Lane are the focus of this study. Lidar data and geomorphic mapping show geomorphic and geometric characteristics consistent with the accommodation of oblique-slip motion along the Wassuk and Smith Valley rangefront faults, while the Mason and Antelope valley rangefront faults appear to be primarily dip-slip. A separate active dextral strike-slip fault in the southernmost part of Mason Valley has likely produced earthquakes in the Holocene. Vertical displacement rates based on cosmogenic ages of displaced alluvial fans for the range-bounding faults in Antelope, Smith, and Mason valleys are $0.5\ ^{+0.5}/_{-0.3}$, $0.5\ ^{+0.7}/_{-0.4}$, and $0.04\ ^{+0.05}/_{-0.03}$ mm/yr, respectively. The vertical rates correspond to dip-parallel slip rates of $0.6\ ^{+0.7}/_{-0.3}$, $0.7\ ^{+1.0}/_{-0.4}$, and <0.05 mm/yr, for the same three faults, respectively, assuming dips on each fault are 55 ± 10°. The along-strike distribution of scarp heights indicates that the most recent and penultimate earthquakes along the range bounding faults of Smith and Antelope valleys produced ~3 m vertical displacements during ~M_w 7 earthquakes. The pattern of faults described here forms a 200-km-long left-stepping en-echelon series of dextral, oblique, and normal faults extending from south of Walker Lake to north of Lake Tahoe, similar to observations of laboratory models of dextral shear.

1 Introduction

1 Introduction

Geodetic observations have brought to light a problem in the Central Walker Lane: while 7–8 mm/yr of northwest directed dextral shear is observed with GPS measurements across this part of the Walker Lane (Thatcher et al., 1999; Hammond and Thatcher, 2005, 2007; Hammond et al., 2011; Bormann et al., 2016), over half of this total shear cannot be accounted for by summing the geologic slip rates of the few known strike-slip faults in this region that is otherwise largely dominated by normal faulting (Wesnousky et al., 2012). We use lidar data to analyze the tectonic geomorphology of Antelope, Mason, and Smith valleys, and a part of the Walker Lake basin to help understand how 7-8 mm/yr of geodetically observed shear is accommodated within the Central Walker Lane between Lake Tahoe and Walker Lake (**Figures 1 and 2**). Boulder and sediment samples from displaced alluvial surfaces are analyzed for terrestrial cosmogenic nuclide (TCN) and optically stimulated luminescence (OSL) to better constrain the slip rates of range-bounding primarily normal faults. This paper summarizes prior work and our new observations bearing on style and rate of faulting for each basin. Here evidence is presented consistent with a model of deformation where left-stepping right-lateral strike-slip faults work in concert with normal faults and transverse left-lateral faults to form a fault system that accommodates significant crustal shear across the Central Walker Lane in the absence of major through-going strike-slip faults.

Field studies and laboratory models show that as strike-slip systems increase in total displacement, the width of the shear zone decreases, while faults become longer, less complex, more continuous, and more efficient at accommodating strain (Wilcox et al., 1973; Aydin and Nur, 1982; Wesnousky, 1988; An and Sammis, 1996; Stirling et al., 1996; Schreurs, 2003;

Faulds et al., 2005; Atmaoui et al., 2006; Zinke et al., 2015; Hatem et al., 2017; Zuza et al., 2017). While many of the transform plate boundaries of the world may be considered mature and capable of producing large earthquakes along well organized fault traces that have accommodated hundreds of kilometers of total slip (e.g., the San Andreas, Altyn Tagh, Sagaing, Denali, or Alpine faults), comparably few immature strike-slip systems have been studied in similar detail (e.g., the Walker Lane, Sicily, the Shan Plateau of Myanmar, or the Shanxi Rift of China). These less well-developed systems have, by this definition, accommodated lesser amounts of total slip, and as a result often lack major through-going faults. Instead these systems form broad regions of faulting and deformation along complex systems of numerous short, discontinuous faults, which are often only capable of producing moderate earthquakes. Studying these complex fault systems in nature offers unique insight into the development of fault systems at a plate boundary scale that can otherwise typically only be understood in a laboratory.

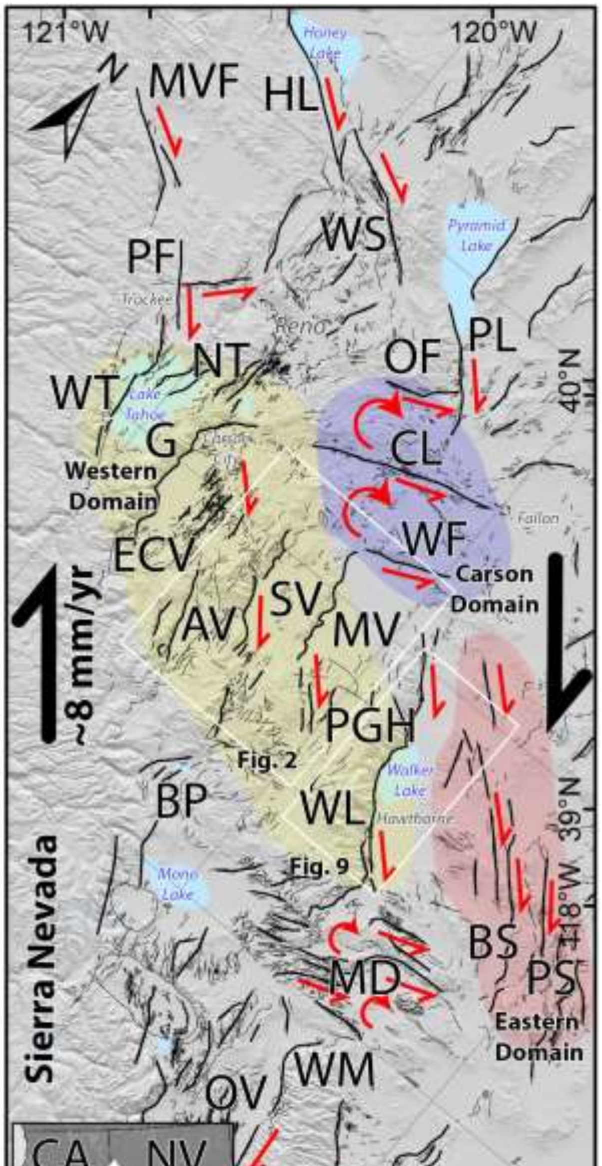

Figure 1 Overview map of Walker Lane. Extent of Figures 2 and 9 are indicated by white boxes. Major faults are thicker while thin faults are from USGS Quaternary fault and fold database. The Central Walker Lane can be divided into the Carson domain (purple), western domain (yellow), and eastern domain (pink). Major faults: MVF- Mohawk Valley, HL-Honey Lake, WS- Warm Springs, PF- Polaris, PL Pyramid Lake, OF-Olinghouse, WT-West Tahoe, NT- North Tahoe (from west to east: Stateline, Incline Village, Little Valley, Washoe Lake), G-Genoa, ECV-East Carson Valley, AV-Antelope Valley, SV-Smith Valley, CL-Carson Lineament, WF-Wabuska, MV-Mason Valley, PGH- Pine Grove Hills, BP-Bridgeport Valley, WL-Walker Lake, BS-Benton Springs, PS-Petrified Springs, MD- Mina Deflection (Rattlesnake, Excelsior, Coaldale), OV-Owens Valley, WM- White Mountains, FLV-Fish Lake Valley.

1.1 Regional Context

The Walker Lane (**Figure 1**) is an approximately 500-km-long by 100-km-wide northwest trending transtensional intracontinental shear zone composed of discontinuous active faults, basins, and mountain ranges that accommodate up to ~20% of the ~50 mm/yr of dextral shear between the Pacific and North American plates (Bennett et al., 2003; Dixon et al., 2000; Thatcher et al., 1999; Unruh et al., 2003). The Walker Lane sits between the Sierra Nevada Mountains to the west and the north-northeast trending normal faults and ranges of the Basin and Range to the east, roughly following the California-Nevada border. The disorganization of faults in the Walker Lane has been cited as evidence of the youthful expression of an incipient transform boundary (e.g., Faulds et al., 2005; Faulds and Henry, 2008). The Walker Lane is well defined geodetically by a zone of ~9 mm/yr of northwest directed right-lateral shear in the southern part, decreasing to ~7 mm/yr in the Northern Walker Lane (e.g., Hammond et al., 2011; Wesnousky et al., 2012; Bormann et al., 2016), while the San Andreas fault system accommodates ~40 mm/yr of dextral shear, west of the Sierra Nevada (Unruh et al., 2003). Throughout the Walker Lane, dextral shear is expressed as transtension, accommodated as strike-slip along well defined faults (e.g., Benton Springs; Wesnousky 2005), as series of left-lateral, transverse “bookshelf faults” (e.g., Cashman and Fontaine, 2000), partitioned into normal faults at range fronts with separate strike-slip faults along the interiors of basins (e.g., Owens Valley; Beanland and Clark, 1994), and has been hypothesized within portions of the Central Walker Lane to be taken up by rotations of crustal blocks bounded by major range-bounding normal faults (e.g., Wesnousky et al., 2012).

The Walker Lane is divided into several regions that display distinctly different fault systems (**Figure 1**). The Northern Walker Lane is composed of the predominantly northwest-striking dextral strike-slip Pyramid Lake (Briggs, 2004; Angster et al., 2016), Warm Springs (Gold et al., 2013), Honey Lake (Gold et al., 2017), Polaris (Hunter et al., 2011), and Mohawk Valley (Gold et al., 2014) faults. The Southern Walker Lane is composed of predominately northwest striking strike-slip and normal faults, including the Owens Valley (Beanland and Clark, 1994; Lee et al., 2001; Kirby et al., 2008; Haddon et al., 2016), Fish Lake Valley (Frankel et al., 2007; Ganev et al., 2010; Frankel et al., 2011), and White Mountains (Stockli et al., 2003; Kirby et al., 2006) faults. The Central Walker Lane interrupts this northwest structural grain with a series of north-striking range-bounding faults with large normal components, transverse left-lateral faults, and some northwest-striking dextral faults.

The Central Walker Lane can be further subdivided into three domains (**Figure 1**). The eastern domain or Walker Lake block is composed of the northwest striking dextral strike-slip Benton Springs, Indian Head, Gumdrop, and Petrified Springs faults(Wesnousky, 2005; Angster et al., 2019). The northerly Carson domain (e.g. Cashman and Fontaine, 2000; Wesnousky, 2005; Li et al., 2017) is composed of the transverse, northeast-striking, sinistral Wabuska, Olinghouse (Briggs, 2005), and Carson faults and lineaments. The western domain is composed of the basins and their range-bounding faults that are the focus of this paper, including the Tahoe (Kent et al., 2005; Maloney et al., 2013; Pierce et al., 2017) and Walker Lake (Bormann et al., 2012; Dong et al., 2014; Surpless and Kroeger, 2015) basins, and Carson (Ramelli et al., 1999; dePolo and Sawyer, 2005), Smith (Wesnousky and Caffee, 2011), Mason, and Antelope (Sarmiento et al., 2011) valleys.

The western domain of the Central Walker Lane is defined by a series of subparallel north-striking/east-dipping active range-bounding faults each dividing a mountain range to the west from a half-graben holding a basin to the east. These north-strike of the ranges contrast sharply with the northeast-striking ranges of the Basin and Range to the east of this region, and the continuous high topography of the Sierra Nevada to the west. Most of these range-bounding faults are ~30–45 km long (except for the ~85 km long Wassuk rangefront fault) and form a rough left stepping en-echelon pattern, with faults spaced ~20–35 km apart from east to west. The westward stratigraphic tilt of these ranges decreases to the northwest from 60° in the Wassuk and Singatse ranges, to <20° in the Carson Range, and <5° in the Sierra Nevada, and likewise the southeasterly Singatse and Wassuk ranges have considerably higher amounts of total extension (>150%) than the ranges to the west (Surpless et al., 2002), which has been cited as evidence of the progressive westward encroachment of faulting into the Sierra Nevada. Thermochronologic data show that many of the mountain ranges in the region have undergone two phases of exhumation: an initial period ~14–15 Ma, and a younger period sometime between 3 and 10 Ma (Surpless et al., 2002). This second phase was initially attributed by Surpless et al. (2002) to be a result of Basin and Range extension, yet this timing coincides with the imitation of the Walker Lane at these latitudes (e.g., Faulds and Henry, 2004), so may be a result of the encroachment of Walker Lane deformation, while the earlier phase may be attributed to Basin and Range extensional faulting (Surpless et al., 2002).

1.2 The problem of missing slip in the Central Walker Lane

Both cumulative lateral displacements and the geodetically measured shear rates across the Walker Lane decrease from south to north. Guest et al. (2007) state that as much as ~110 km of right-lateral slip has been accommodated across the Stateline, Owens Valley, Panamint Valley, and Death Valley-Fish Lake Valley faults of the Southern Walker Lane since the mid-Miocene. In the Northern Walker Lane, Faulds et al. (2005) show that only ~20–30 km of net dextral shear has been accommodated by strike-slip faults. Cashman and Fontaine (2000) and Carlson (2017) present paleomagnetic evidence of >50° of clockwise vertical axis rotations that have accumulated in some of the Miocene volcanic rocks of the Carson domain. Across the Central Walker Lane, GPS profiles measure ~7–8 mm/yr of northwest directed dextral shear (Hammond et al., 2011; Wesnousky et al., 2012; Bormann et al., 2016). This magnitude of shear and rotation appears to have been largely accommodated in the absence of major through going northwest-directed dextral strike-slip faults in the western domain of the Central Walker Lane, and as Wesnousky et al. (2012) show, profiles can be drawn perpendicular to the trend of the Walker Lane without crossing any major faults in the Central Walker Lane.

Optimally-oriented, closely-spaced right-lateral strike-slip faults of the Walker Lake block of the Central Walker Lane accommodate ~4 mm/yr of dextral shear (Angster et al., 2019). Aside from a short fault segment observed along the eastern margin of the Wassuk Range (Dong et al., 2014), there are no previously reported right-lateral strike-slip faults in the western or Carson domains that accommodate the remaining >3 mm/yr of dextral shear. GPS transects show that the observed shear is evenly spaced across the Central Walker Lane, and is not isolated to the Walker Lake block (Bormann et al., 2016).

Wesnousky et al. (2012) suggested that range scale block rotations and asymmetric, northward-opening basins accommodate the observed geodetic shear across the western domain of the Central Walker Lane. Geodetic block models (e.g. Bormann et al., 2016) suggest that as much as ~1.5 mm/yr of dextral oblique slip is accommodated by each of these range-bounding normal faults, in addition to clockwise vertical axis rotations of crustal blocks. However, the paleomagnetic work of Carlson (2017) suggests that while significant block rotations have occurred in the Carson domain, there has been little rotation of the ranges in the western domain. Thus, strike-slip faulting in the western domain may play a larger role in accommodating Walker Lane shear than has been previously recognized. Such strike-slip faulting may be either (1) diffused across scattered, discontinuous faults (similar to the 1932 M_s 7.2 Cedar Mountain earthquake, e.g., Bell et al., 1999), (2) accommodated by off-fault deformation that is not preserved or readily observed by available paleoseismic methods (e.g., Gold et al., 2015; Personius et al., 2017), or (3) accommodated along previously unrecognized major strike-slip faults (e.g., Dong et al., 2014), all of which are hypotheses addressed in this paper.

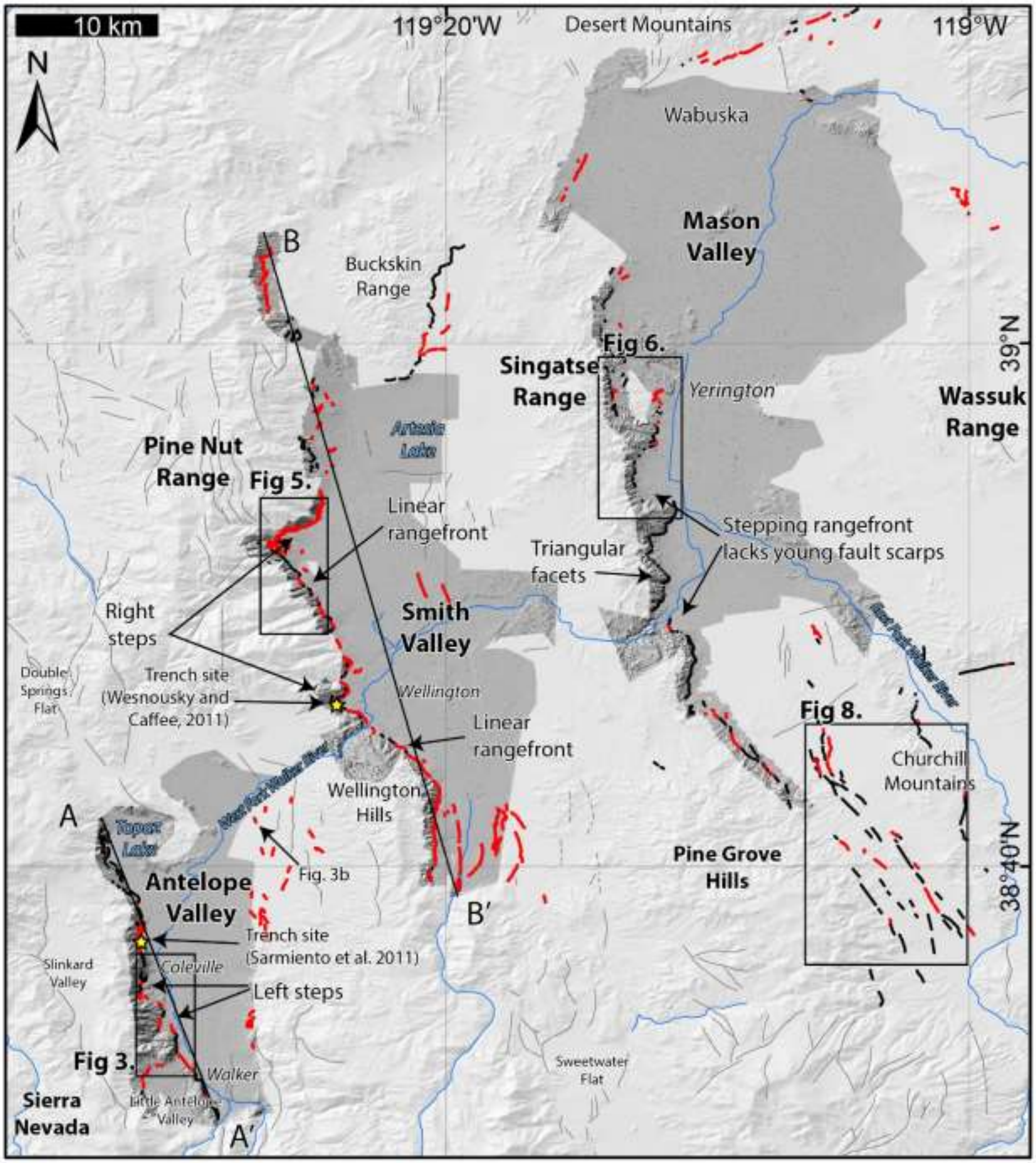

Figure 2 Overview of study area. Dark grey hillshades indicate extent of lidar data. Red lines are faults mapped in this study and observed cutting alluvial deposits, and dark black faults are bedrock-alluvial active fault contacts. Light black lines are faults from USGS Quaternary fault and fold database. Black boxes indicate the extent of Figures 3, 5, 6, and 8. Profiles A-A' and B-B' are plotted in Figure 10.

2. Resources and Methods

2.1 Quaternary mapping and high resolution topographic data sources

Descriptions of faulting characteristics along each of the faults and lineaments are derived from the analysis of large-scale (~1:12,000) low-sun-angle black and white aerial photographs, Google Earth satellite imagery, structure-from-motion models, and lidar data (three existing datasets from the USGS, Desert Research Institute, and National Wildlife Service are merged with the ~334 sq km of new data that was acquired for this project through the National Center for Airborne Laser Mapping). Lidar datasets are merged into a seamless dataset for each basin and then contour, and hill- and slope-shade maps are generated for geomorphic analysis. Structure-from-motion elevation models are generated using Agisoft Photoscan Pro with images collected using a DJI Phantom 3+ quadcopter. Images are georeferenced from sites located in a target region using a Trimble R10 dGPS unit, resulting in ~25 cm/pixel resolution models.

Generalized surficial maps based on interpretations of lidar data and satellite imagery at a scale of 1:12,000 are constructed for Mason, Smith, and Antelope valleys using a modification of the methods outlined in Bull (1991) as used in various other studies in this region (e.g., Bell et al., 2004; Wesnousky, 2005; Koehler and Wesnousky, 2011; Sarmiento et al., 2011; Wesnousky and Caffee, 2011; Li et al., 2017). In **Plate 1** and the derivative figures in this paper, deposits are divided into units based on relative age and type of geomorphic landform/sediment: fluvial (Qfl), basin fill (Qbf), playa/lacustrine (Qp), aeolian (Qd), and four alluvial fan units (Qa, Qy, Qi, and Qo). Land obscured by anthropogenic activity (anth) and undivided bedrock (bx) are also mapped. Alluvial fan units are divided by relative age primarily using height above modern stream grade, amount of dissection, height of fault scarp (if present), and textural differences in imagery and lidar data. Fault traces in this paper are divided as either fault scarps that are clearly expressed in Quaternary deposits (red lines) or as inferred faults and/or fault contacts between Quaternary deposits and bedrock (black lines).

Surfaces of the oldest alluvial fan units (Qo) are composed of weathered boulders with soils that have well-developed Bt and carbonate horizons. These form the highest and oldest alluvial fan units that are often incised >10 m with well-rounded interfluves. These Qo alluvial fans are considered to be early to middle Pleistocene. Intermediate alluvial fans (Qi) are moderately incised with well-developed drainage networks and are modified by shoreline deposits when near the high stand of Lake Lahontan. Qi alluvial fans are considered middle to late Pleistocene in age. Qy alluvial fans are low lying, and have smooth surfaces in lidar, and a dark tone in imagery. Qy alluvial fans are Holocene and latest Pleistocene. Qa alluvial fans represent active washes and alluvial fans, and are differentiated from Qy alluvial fans by lighter tone on imagery and well-defined channel morphology. Where faults are present, Qy alluvial fans are sometimes differentiated from Qa alluvial fans by fault scarps that do not cut the younger Qa alluvial fans.

2.2 Geochronology

Surficial ages are estimated using measurements of in-situ terrestrial cosmogenic nuclide (TCN) ^{10}Be and ^{36}Cl concentrations of surface boulders, TCN ^{10}Be concentrations of soil depth profiles, and optically stimulated luminescence (OSL) of buried sand lenses. Both ^{10}Be and ^{36}Cl concentrations are measured at the PRIME lab at Purdue. All ^{10}Be samples are processed in the

Geochronology Laboratories at the University of Cincinnati following the methods of Kohl and Nishiizumi (1992). The OSL analyses are also performed at the University of Cincinnati. The ^{36}Cl samples are processed and analyzed at the PRIME lab. Detailed descriptions of sample preparation and analysis are in the Supporting Information.

Boulder sampling focuses on the largest boulders from alluvial fan surfaces. Approximately 500 g samples are taken from the upper 2–5 cm of each of these boulders. Photographs of each of the sampled boulders are provided in the Supporting Information. ^{10}Be concentrations and laboratory data are listed in **Table S1.** The ^{10}Be TCN boulder exposure ages are calculated using the Cosmic Ray Exposure Program (CREp) of Martin et al. (2017) and are listed in **Table 1**. The ages reflect the increased concentrations of ^{10}Be that occur in rock as a function of the time they are exposed to cosmic rays at Earth's surface. The calculator requires input describing the geographic coordinates and elevation of the samples, local shielding of the sample, density of the sample, and estimation of the boulder erosion rates resulting from processes such as boulder grussification and spalling (Gosse and Phillips, 2001). These values are listed for each sample in **Table S1**. The calculations are made using no erosion rate. The age estimates are also dependent on the assumption of particular scaling models designed to estimate the long-term production rate of cosmogenic ^{10}Be. The ^{10}Be ages in **Table 1** use a production rate of 44.0 ± 0.3 at/g SiO_2/yr determined at Twin Lakes, which is located at a higher elevation than the fan surfaces here, but is within 100 km of all study sites (Balco et al., 2008; Borchers et al., 2016; Nishiizumi et al., 1989), the ERA40 atmosphere model of Uppala et al. (2005), the Lifton-VDM2016 geomagnetic database (Lifton, 2016), and the time-dependent scaling model of Lal (1991) and Stone (2000). The ^{36}Cl boulder ages are calculated using the CRONUS calculator for ^{36}Cl, and are listed in **Table 1**, with laboratory details in **Table S2.**

To determine the age of a surface using a cosmogenic depth profile, a ~2-m-deep profile is excavated and the exposed sediment is sampled at varying depths for ^{10}Be analysis. The resulting ^{10}Be concentrations as a function of depth are modeled using the Hidy et al. (2010) MATLAB code, which uses a Monte-Carlo simulation to find the best fit of the data and resulting surface age. Soil textural grain size analysis is performed by A&L Great Lakes Laboratories, Inc.

OSL samples are extracted using 20-cm-long plastic tubes from sand lenses exposed in a hand excavated pit. All tubes are packed and wrapped double-bagged in opaque media for transport. OSL samples are processed and analyzed at the luminescence dating laboratories at the University of Cincinnati in subdued sodium lighting (588 nm). Quartz grains are isolated from heavy minerals and feldspars using pretreatment with H_2O_2, HCl and HF, and magnetic separation. Modified single-aliquot regeneration (SAR) protocols (Wintle and Murray, 2006) were employed on small aliquots (200–500 grains; 100–150 µm in diameter) to estimate equivalent doses using a Risø OSL DASH measurement system. U, Th, Rb, and K are measured at Activation Laboratories Limited Ancaster, Ontario Canada to determine sediment dose rates and estimations of the contribution of cosmic dose rate accounted for geographic position, elevation, and depth, burial depth, and water content as outlined in **Table S3**.

2.3 Scarp height measurements

Fault scarp vertical heights are determined by extracting topographic profiles from lidar data. Topographic profiles are extracted approximately orthogonal to fault scarps where both hanging and footwall surfaces are similar and show minimal to no modification by geomorphic and anthropogenic processes unrelated to faulting (e.g., road cuts, younger fan deposition, fluvial modification, etc.). Profiles are analyzed using a python code written for this study (see Supporting Information) that fits linear regressions to points selected by the user that are representative of the hanging wall, foot wall, and fault scarp surfaces. The vertical separation between the footwall and hanging wall regressions is then measured at the horizontal midpoint of the intersections between the fault scarp and each of the hanging and foot walls (e.g. Rood et al., 2011).

2.4 Slip Rate Calculations

Vertical slip rates are determined by dividing the probability distributions of the displacement of a surface by the age of the displaced surface using the MATLAB code of Zechar and Frankel (2009). The probability distribution of the age of a surface is the sum of the uncertainties of all of the samples from a single surface. This approach is taken to reduce the uncertainty of scattered sample ages resulting from inheritance or erosion. With this method all samples are treated equally. The uncertainty of the displacement is assumed to be Gaussian, described by the mean and standard deviation of the scarp heights of a number of profiles extracted perpendicular to a fault scarp in a deposit of a single age. A Gaussian distribution is used to better estimate the actual average fault offset from a number of measurements of fault scarps, modified unknown amounts by erosion on the hanging wall, deposition on the footwall, and the natural variability of the earthquake displacement along fault strike. The approach is thus aimed at determining an “average” slip rate, rather than a maximum or minimum bound, along a particular fault section where numerous measurements of age and displacement are recorded.

3. Study Areas

3.1 Antelope Valley

Antelope Valley is a west tilted half-graben with a northwest striking, east-dipping active rangefront fault along its western margin separating the basin from the mountains to the west (**Figure 2**). The West Fork of the Walker River flows from south to northeast through the basin, generally following the western side, and likely obscuring any long-term evidence of faulting along its path within the valley. The rangefront exhibits frequent, prominent triangular facets, and forms ~800 m of relief above the valley floor. While the overall trend of the fault follows a ~23-km-long northwest trace, fault scarps are only expressed in intermediate and young alluvial deposits for ~15 km of that length, and generally form a left-stepping pattern of discontinuous mostly north-trending fault scarps **(Figure 3)**. Fault scarps in late Quaternary alluvial deposits that range in height from ~1–3 m to >20 m commonly occur at the mouths of drainages (**Figure 3**), demonstrating the repetition of late Quaternary earthquakes. Topaz Lake obscures any evidence of the rangefront fault along the northwestern portion of Antelope Valley. North of Topaz Lake, and outside of our lidar data, there are discontinuous scarps approaching Double-Springs Flat (**Figure 2**).

3.1.1 Walker Slip Rate Site

A large uplifted alluvial fan terrace is present just northwest of the town of Walker (**Figure 3**). Five profiles measured across different parts of the fault scarp at this site (**Figure 3c**) have vertical separations ranging from 21.3 to 32.5 m, with a mean value of 27.5 ± 4.3 m. The surface here forms an ~1-m-thick alluvial cap exhibiting numerous boulders on a bedrock pediment surface that is incised over 20 m by drainages (**Figure 3c).** The faulted surface exhibits a bench of slightly lower elevation adjacent to the fault. The surface of this bench contains a thin scattered rounded cobble deposit that was likely deposited by the Walker River. Not only does the scarp itself appear to be modified by the Walker River, but the lower surface here is buried by younger fan activity and fluvial deposition from the nearby Walker River, and thus this measured displacement is a minimum. Boulders on the Qi surface here are heavily weathered, mostly volcanic rocks sourced from the nearby Sierra Nevada. Here, we collected six boulder samples for ^{36}Cl cosmogenic analysis (**Table 1**). Resulting ages range from 33.3 to 111.0 ka (**Figure 3c**). Combining the average vertical separation with this age distribution results in a vertical separation rate of 0.5 $^{+0.5}/_{-0.3}$ mm/yr (**Figure 4**). The section of rangefront immediately adjacent and north of this site is composed of a several hundred meter tall granite bedrock escarpment with slopes ranging from 50 to >70° (**Figure 3a**), which may reflect a steep dip of the range front fault.

3.1.2 Faulting in east Antelope Valley

The east side of the basin contains a series of uplifted, faulted, and tilted alluvial surfaces that appear to grade into pediment surfaces extending westward from the crest of the Wellington Hills (**Figure 2**). The surfaces are mostly outside of the extent of the available lidar data. Google Earth imagery shows a series of discontinuous both north and northwest trending fault scarps. Many of the fault scarps are uphill (east) facing with some exhibiting right-lateral deflections of drainages, which may be a result of strike-slip faulting. The alluvial surfaces in the eastern part of the valley are incised by numerous small drainages and appear to be intermediate and old (**Plate 1**). The scarps within the surfaces are generally small and likely do not rupture frequently.

At one location in eastern Antelope Valley a channel incised into a broad Qi alluvial fan is obliquely cut by a short ~300-m-long fault trace of relatively weak geomorphic expression (**Figure 3b**). The fault forms a slight (~0.5 m) uphill-facing fault scarp in the Qi fan and appears to laterally displace this channel ~70 m. Three samples were extracted from sand lenses exposed in a pit dug into the Qi surface and were dated using OSL. Samples EA1 and EA2 were saturated, with a likely age of >51 ka, and EA3 resulted in an age of 56.6 ± 5.2 ka. Combining this minimum age of 56.6 ± 5.2 ka with this displacement of ~70 m results in a maximum right-lateral slip rate of 1.2 ± 0.4 mm/yr. The estimated slip rate seems anomalously high in relation to the short length of the fault strand, the relatively weak geomorphic expression of the scarp, and the lack of offsets in the younger deposits farther along strike closer to the Walker River. Nonetheless, we present the observation to illustrate the only possible direct evidence we observed for strike-slip motion along the east side of the valley. If this >57 ka age is assumed for the rest of the Qi alluvial fan surfaces in eastern Antelope Valley, then the lack of geomorphic expression of significant faulting suggests that the few discontinuous fault scarps here are not accommodating a significant amount of the regional strain.

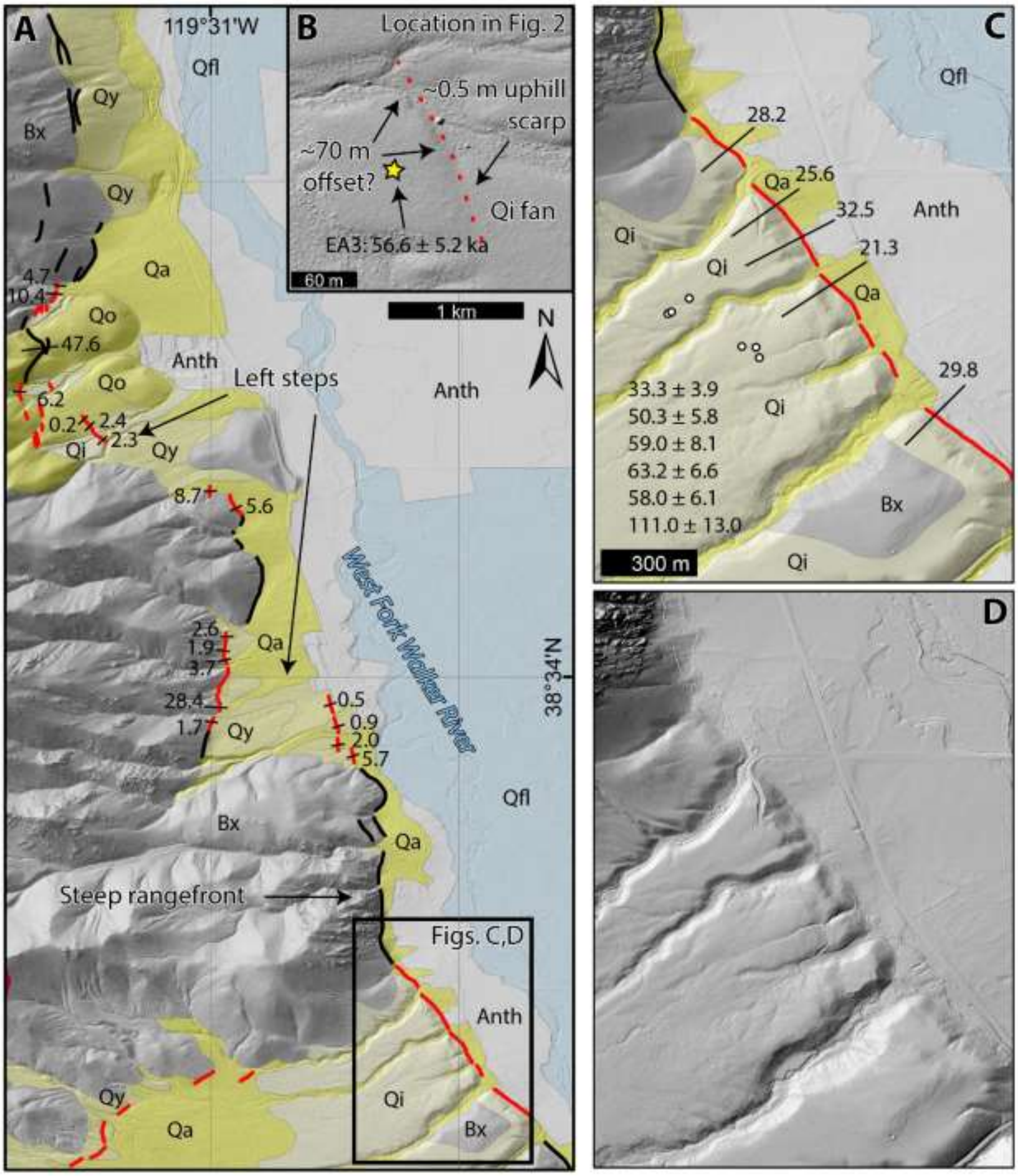

Figure 3 Section of Antelope Valley rangefront showing left-stepping pattern (aA) and location of Walker slip rate site (c). (b) is a section of eastern Antelope Valley (location in Fig. 2) where a Qi alluvial fan is apparently offset ~70 m. Location of OSL samples EA1-3 with minimum age of 56.6 ± 5.2 ka are indicated. Black faults are bedrock-alluvial fault contacts. Red faults are fault scarps in alluvial deposits. Straight black lines are scarp profiles and values are scarp heights in (m). Walker slip rate site interpreted (c) and bare lidar hillshade (d). Scarp profiles (black lines), heights (in m), and ages (ka) of boulder samples (white dots) are shown in (c).

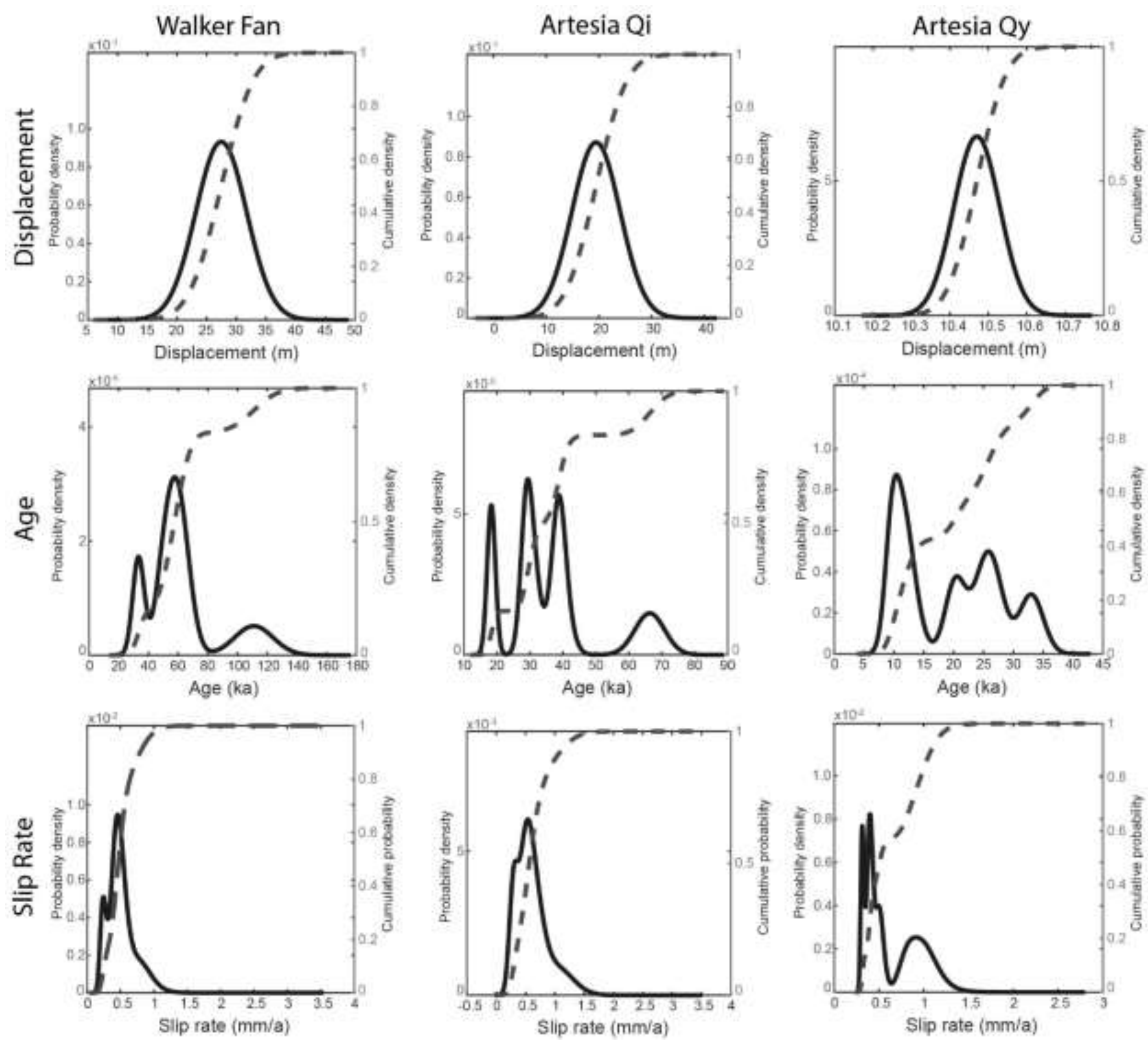

Figure 4 Displacement, age, and vertical slip rate probability distributions for the Antelope Valley and Smith Valley range bounding faults. For each plot, probability densities are the solid lines (left axis), while cumulative probabilities are the dashed lines (right axis).

Table 1. Geochronology. Details are in Supporting Information

TABLE 1. GEOCHRONOLOGY

Method	Sample name	Location		Elevation	Age	1σ error
		latitude	longitude	above sea level		
		(ºN)	(ºW)	(m)	(ka)	(ka)
Mason Valley	*Upper Yerington Fan*					
^{10}Be Boulder	MVS1	38.9669	119.2012	1424	451.1	37.2
^{10}Be Boulder	MVS2	38.9661	119.2019	1430	93.3	6.6
^{10}Be Boulder	MVS3	38.9660	119.2034	857	183.5	13.5
^{10}Be Boulder	MVS4	38.9653	119.2028	1431	90.5	6.9
^{10}Be Depth Profile	M1-Pit	38.9669	119.2012	1425	173.1	$^{38.7}/_{-32.5}$
Smith Valley	*Artesia Fan - intermediate surface*					
^{10}Be Boulder	SF1	38.8908	119.4158	1494	30.2	2.6
^{10}Be Boulder	SF2	38.8909	119.4163	1497	19.3	1.6
^{10}Be Boulder	SF3	38.8903	119.4158	1491	40.4	2.8
	Artesia Fan - intermediate surface (Wesnousky and Caffee, 2011)					
^{10}Be Boulder	CWL-2	38.8907	119.4150	1480	32.5	3.0
^{10}Be Boulder	CWL-3	38.8907	119.4148	1470	40.7	3.7
^{10}Be Boulder	CWL-4	38.8907	119.4148	1480	69.9	6.3
	Artesia Fan – upper younger surface					
^{10}Be Boulder	SF4	38.8892	119.4164	1494	21.3	2.0
^{10}Be Boulder	SF5	38.8892	119.4165	1494	12.1	1.7
^{10}Be Boulder	SF6	38.8893	119.4171	1500	34.7	2.9
	Artesia Fan - lower younger surface					
^{10}Be Boulder	SF8	38.8892	119.4149	1468	27.4	2.6
^{10}Be Boulder	SF9	38.8892	119.4148	1472	26.6	3.0
^{10}Be Boulder	SF10	38.8894	119.4145	1458	13.4	2.1
^{10}Be Boulder	SF11	38.8888	119.4142	1450	10.3	1.3
Antelope Valley	*Walker Fan*					
^{36}Cl Boulder	CWL-5	38.54039	119.5023	1654	58.0	6.1
^{36}Cl Boulder	CWL-6	38.54071	119.5025	1650	111.0	13.0
^{36}Cl Boulder	CWL-7	38.54069	119.5024	1649	59.0	8.1
^{36}Cl Boulder	CWL-8	38.54164	119.5049	1657	63.2	6.6
^{36}Cl Boulder	CWL-9	38.54169	119.5048	1659	50.3	5.8
^{36}Cl Boulder	CWL-10	38.54208	119.5043	1654	33.3	3.9
	East Antelope Fan					
OSL	EA1-160	38.695538	119.45527	1580	>51	-
OSL	EA2-140	38.695538	119.45527	1580	>51	-
OSL	EA3-120	38.695538	119.45527	1580	56.6	5.2

374

3.2 Smith Valley

Smith Valley is a half-graben with a NNW-striking active rangefront fault bounding the Pine Nut Range to the west **(Figure 2)**. The half graben is ~50-km-long, and 15-km-across at its widest. The total vertical relief from the valley floor to the crest of the Pine Nut Range is over 1400 m. The West Fork of the Walker River enters Smith Valley through a narrow canyon near the town of Wellington (**Figure 2**). It bends northeastward here and meanders across the basin through a canyon of increasing depth before it exits the valley on the eastern side, cutting through the Singatse Range. This canyon is cut into lacustrine and fluvial deposits, likely deposited by Pluvial Lake Wellington, which reached a highstand of 1477 m above sea level (asl) between 60 and 80 ka (Stauffer, 2003; Wesnousky and Caffee, 2011). In the central part of the basin, just north of the Walker River, there are a pair of left-stepping, north striking, en-echelon fault strands that form 1–2-m-high scarps in stabilized aeolian/dune deposits (**Figure 2**). The faults do not cut any of the younger floodplain deposits closer to Walker River. Artesia Lake, a small playa remnant of pluvial Lake Wellington (Stauffer, 2003), is present in the northern part of Smith Valley, and is hydrologically isolated from the Walker River.

The range bounding fault in Smith Valley forms an abrupt rangefront with triangular facets, scarps in young alluvial fans, and uplifted alluvial terraces. The rangefront fault generally strikes northwest and makes several northeast-striking right steps separating otherwise long, northwest striking linear sections (**Figure 2**). When the strike of the fault changes from north-northwest to northeast within these right-steps, both the frequency of scarps and their heights increase dramatically from less frequent ~6–8-m-high scarps in the linear NNW sections to >20-m-scarps along the largest of these northeast striking step overs near the Artesia Fan **(Figure 5)**. The fault primarily exhibits down to the east/southeast vertical displacement, and nowhere did we observe laterally displaced stream channels recording right-lateral strike-slip motion. The faulting in the southernmost portion of the basin near the Wellington Hills forms a horsetail splay (**Figure 2**) of numerous large (~5–10-m-high) scarps. These scarps are generally sub-parallel to the northward drainage of the basin in this area and thus may be modified by fluvial processes. The northern portion of Smith Valley is occupied by the Buckskin Range, which is bounded by an active fault on its east flanks. This fault forms a fairly continuous north-northeast striking scarp in young, intermediate, and older alluvial fan deposits. To the west of the Buckskin Range, there is a continuation of the Smith Valley rangefront fault, and here we observe frequent grabens, en-echelon fault scarps, and vertically displaced Holocene Qy alluvial deposits.

3.2.1 Artesia Fan slip rate site

At the eastern edge of a ~1.4-km-long right-step over in the north-northwest striking rangefront fault **(Figure 5)**, older fan surfaces exhibit progressively larger vertical scarps than younger surfaces. Three alluvial fan surfaces are mapped in **Figure 5b:** Qa are the active alluvial fan deposits, forming a narrow active channel cut into young Qy deposits, and on the basin floor form a small fan overtopping Qy deposits. These Qy deposits form an alluvial fan on the hanging wall of the fault as well as on the margins of the main Qa channel on the footwall, and are composed of light gray, rounded, unweathered granitic boulders in a poorly-sorted matrix. Intermediate Qi deposits are only found on the footwall of the fault and are redder in color, with a smoother, less bouldery surface than Qy. The fault has an anastomosing pattern in **Figure 5b** that, from south to north, starts as a single strand, splits into two, then three strands, before coalescing into a single strand again. A maximum age of the Qi fan here is constrained by a 60–80 ka tephra exposed in a road cut in the fault scarp (Stauffer, 2003; Wesnousky and Caffee, 2011). We collected 10 boulder samples for ^{10}Be analysis on the Qi and Qy displaced alluvial fan units and combined these with 3 recalculated ^{10}Be boulder ages at this site from Wesnousky and Caffee (2011) (**Figure 5b**). Six boulder samples were collected from the footwall of the intermediate unit (Qi, **Figure 5b**), and range in age from 18 to 66 ka (mean age of 37.0 ± 16.3 ka), and seven samples from both the hanging and footwalls of a younger aged alluvial fan unit (Qy, **Figure 5b**) range in age from 10 to 33 ka (mean age of 19.7 ± 8.9 ka) (**Table 1**). While these ages are scattered, the mean ages of the young surface are roughly half of that from the intermediate surface. The average of four profiles measured from the available lidar data (**Figure 5**) show that scarp height in the single strand that cuts the intermediate unit is 19.5 ± 4.5 m, while two profiles of each of the two scarps in the younger unit measure 3.8 ± 0.1 and 6.6 ± 0.2 m, respectively, or 10.5 ± 0.1 m combined (**Figure 5**). Dividing these scarp heights by the ages of the boulder samples from each surface leads to a vertical separation rate of 0.6 $^{+0.8}/_{-0.2}$ mm/yr for the intermediate surface and 0.5 $^{+0.7}/_{-0.2}$ mm/yr for the young surface **(Figure 4)**. The two rates over different timescales generally agree.

Both the linearity and strike of the long northwest striking segments of the rangefront in Smith Valley suggest that a component of strike-slip is accommodated along the rangefront fault. The Artesia fan is located on the edge of the largest right-step in the Smith Valley rangefront, where scarps are both more frequent and larger than elsewhere along the rangefront (**Figure 5**), and the strike in this step is nearly perpendicular to the primary northwest strike of the rangefront. In a right-lateral fault system, right-steps produce extension parallel to the trace of the right-lateral fault (**Figure 5d**). The vertical displacement at the Artesia Fan is attributed to the kinematics of a right-step in a northwest striking fault with a large component of right-lateral strike-slip. For an obliquely slipping rangefront like Smith Valley, a low rate of lateral-slip may lead to the burial/obfuscation of possible geomorphic indicators of discrete lateral earthquake offsets.

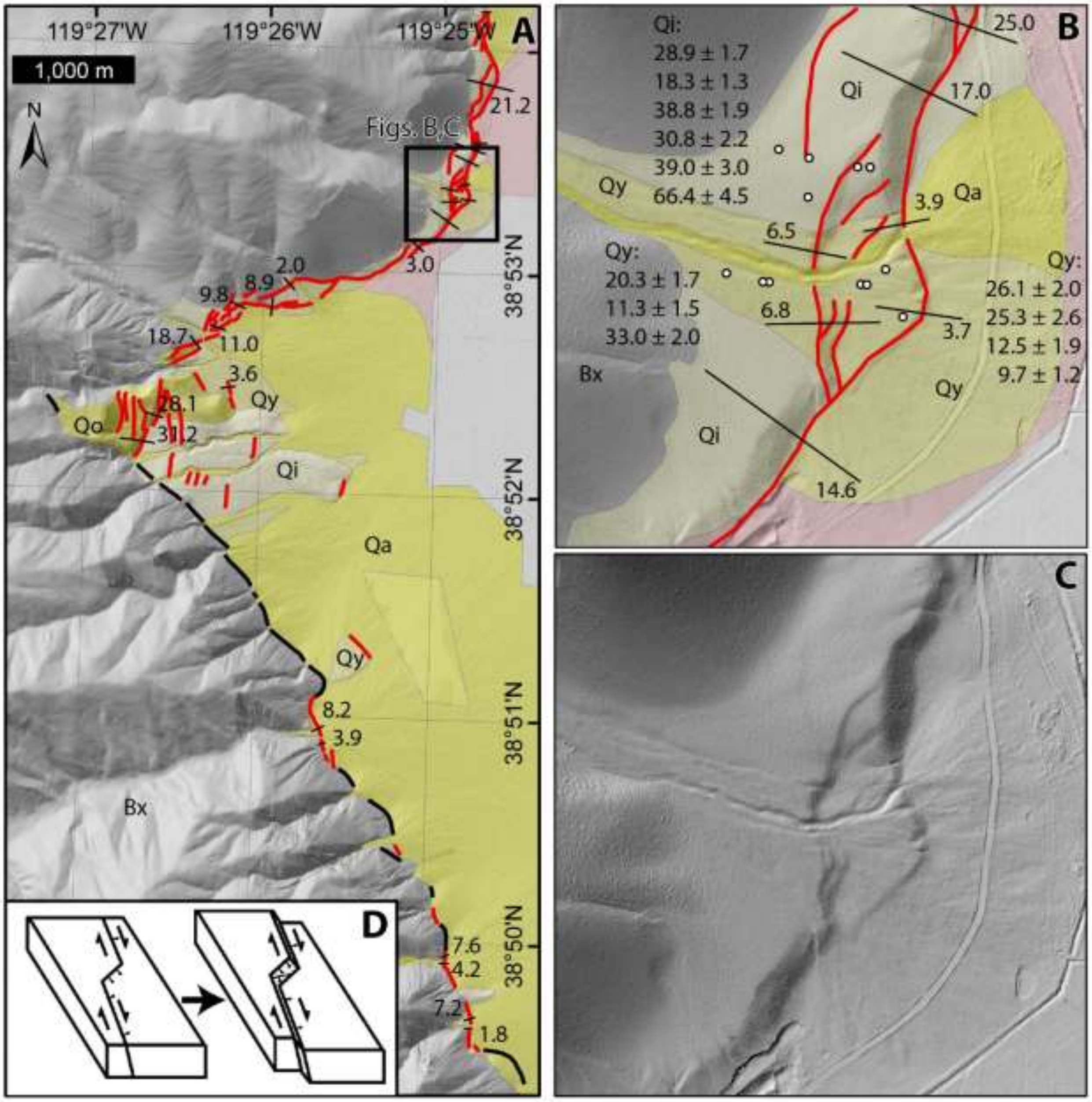

Figure 5 Section of Smith Valley rangefront showing geometry of large right step (a) and location of Artesia fan slip rate site (b, c). Black faults are bedrock-alluvial fault contacts, while red faults are fault scarps in alluvial deposits. Values in (a) are scarp heights (in m). Artesia fan rate site interpreted (b) and bare lidar hillshade (c). Scarp profiles, heights (in m), and ages (ka) of boulder samples (white dots) are shown in (b). (d) Simplified block diagram of a right-bend in a right-lateral oblique fault system provided to explain relatively larger vertical displacements in the step.

3.3 Mason Valley

Mason Valley is a 55-km-long by 20-km-wide half-graben bounded by active faults separating the basin from the Singatse Range to the west and the Pine Grove Hills to the southwest **(Figure 2)**. The Desert Mountains bound the northern margin of Mason Valley where the northeast-striking left-lateral Wabuska fault is located (Li et al., 2017). The Singatse Range is considerably smaller in topographic expression than the other ranges in this region, forming only ~700 m of relief above the valley floor. The northern portion of the basin was occupied by pluvial Lake Lahontan during its high stand ~14.5 ka (Adams and Wesnousky, 1998; Reheis, 1999), and prominent wave-cut shoreline benches and beach deposits are preserved on Qy deposits that are below the ~1332 m elevation of the high stand. Evidence for any pre-Holocene faulting in much of the northern portion of the basin may be obscured by lacustrine processes associated with Lake Lahontan and evidence of more recent faulting in the central portion of the basin may be obscured by agricultural activity.

The region to the east/southeast of Mason Valley, and east of the Churchill Mountains in **Figure 2**, forms a series of complicated small basins and mountain ranges composed of incised Qi aged and older fan/pediment surfaces, short discontinuous faults, and disrupted bedrock **(Plate 1)** (Gilbert and Reynolds, 1973). These basins are both oriented north-south and east-west. The faults in this part of the basin strike both north-northwest and east-northeast, and are generally only traceable for a maximum of ~5 km.

The fault at the base of the Singatse Range forms a sinuous trace with frequent left and right steps and bends from ~5 km south of where the west fork of the Walker River enters the basin for ~35 km northward (**Figure 2**). The Singatse range front is composed of prominent triangular facets, suggestive of active normal faulting, however the fault along the Singatse Range is almost always only expressed as a bedrock alluvium contact, except for the site described in the following section, and forms a sharp contrast with other major range bounding faults in the area that often exhibit scarps in young alluvial deposits. In several places along the rangefront small antithetic grabens are observed, yet there is a dearth of uplifted fan surfaces.

The character of rangefront faulting in Mason Valley abruptly changes ~5 km south of where the west fork of the Walker River enters the southwestern margin of the basin (**Figure 2**) The southern part of the basin is bound by the Pine Grove Hills, and instead of forming a rangefront composed of sharp triangular facets, the rangefront is subdued and is composed of a series of uplifted old alluvial fans and pediments. Here, satellite imagery and lidar data show a discontinuous series of linear, northwest-striking faults and lineaments that extend for ~22 km until the southernmost extent of the basin. Generally these faults have a northeast down sense of motion, and locally right-laterally displace fan deposits and channels.

3.3.1 Yerington Fan slip rate site

Adjacent to the Yerington Pit (**Figure 6**) a northwest striking fault scarp merges with a northeast striking fault scarp to form a large northeast striking graben cutting intermediate age alluvial fan deposits (**Figure 6**). The alluvial fan is incised up to ~6 m by channels and forms broad smooth interfluve surfaces with infrequent highly weathered granitic and volcanic boulders. Depending on where fault profiles are measured (**Figure 6**), vertical separation varies from as little as 1.4 m across the graben at the northeastern extent of the fault scarp to as much as

10.8 m, with an average of 6.5 ± 3.6 m for the 6 profiles. Here, we collected a depth profile of 4 samples as well as 4 surficial boulder samples for cosmogenic ^{10}Be analysis to constrain the age of the faulted surface. Boulder ages sampled from the Qo surface here range from 90.5 ± 6.9 ka to 451.1 ± 37.2 ka with a mean of 204.6 ± 169.9 ka, and modeling the depth profile results in an age of 173.1 $^{+38.7}/_{-32.5}$ ka (**Figure 7**). The well-developed soil, with a thick Bt horizon, (**Figure 7b**) is consistent with the modeled age of the depth profile. Combining the 173.1 $^{+38.7}/_{-32.5}$ ka age of the depth profile with the 6.5 ± 3.6 m average displacement of the surface results in a vertical slip rate of <0.04 mm/yr. The geometry of the linear northwest striking fault segment associated with a large northeast striking graben is consistent with northwest-directed dextral motion, however the measured slip rate is very low and thus this fault does not likely accommodate a significant amount of the regional strain.

3.3.2 Pine Grove Hills fault zone

Figure 8a is a Google Earth satellite image of a portion of the southern part of Mason Valley (**Figure 2**). Here, several subparallel fault traces are well expressed as a series of linear bedrock ridges and scarps in different ages of alluvial fans (**Plate 1**). The linear bedrock ridges are primarily composed of Mio-Pliocene sedimentary and volcanic rocks, including the Morgan Valley and Coal Valley formations (Gilbert and Reynolds, 1973). **Figure 8b** is a Quaternary map based on a hillshade of a 0.25 m/pixel resolution structure-from-motion model of a part of one of these northwest striking fault-lineaments, where a linear fault trace right-laterally displaces Qy and Qi deposits. Two Qi terrace risers are displaced ~25 and ~18 m right-laterally, and a channel is dextrally offset ~20 m by this fault. Additionally along the strike of this fault are two beheaded channels, two right-laterally deflected channels, and a small shutter ridge (**Figure 8b).** Additionally, the direction of the scarp produced by the fault changes from west facing, to east facing, to west facing again along strike, demonstrating the strike-slip nature of this fault. The morphology of the Pine Grove Hills fault is similar to other active strike-slip faults in the region with slip rates ranging from ~0.5 to 1.5 mm/yr (e.g., Wesnousky, 2005; Angster et al., 2019). No age estimates of the offset surfaces are available to determine a slip rate for the Pine Grove Hills fault.

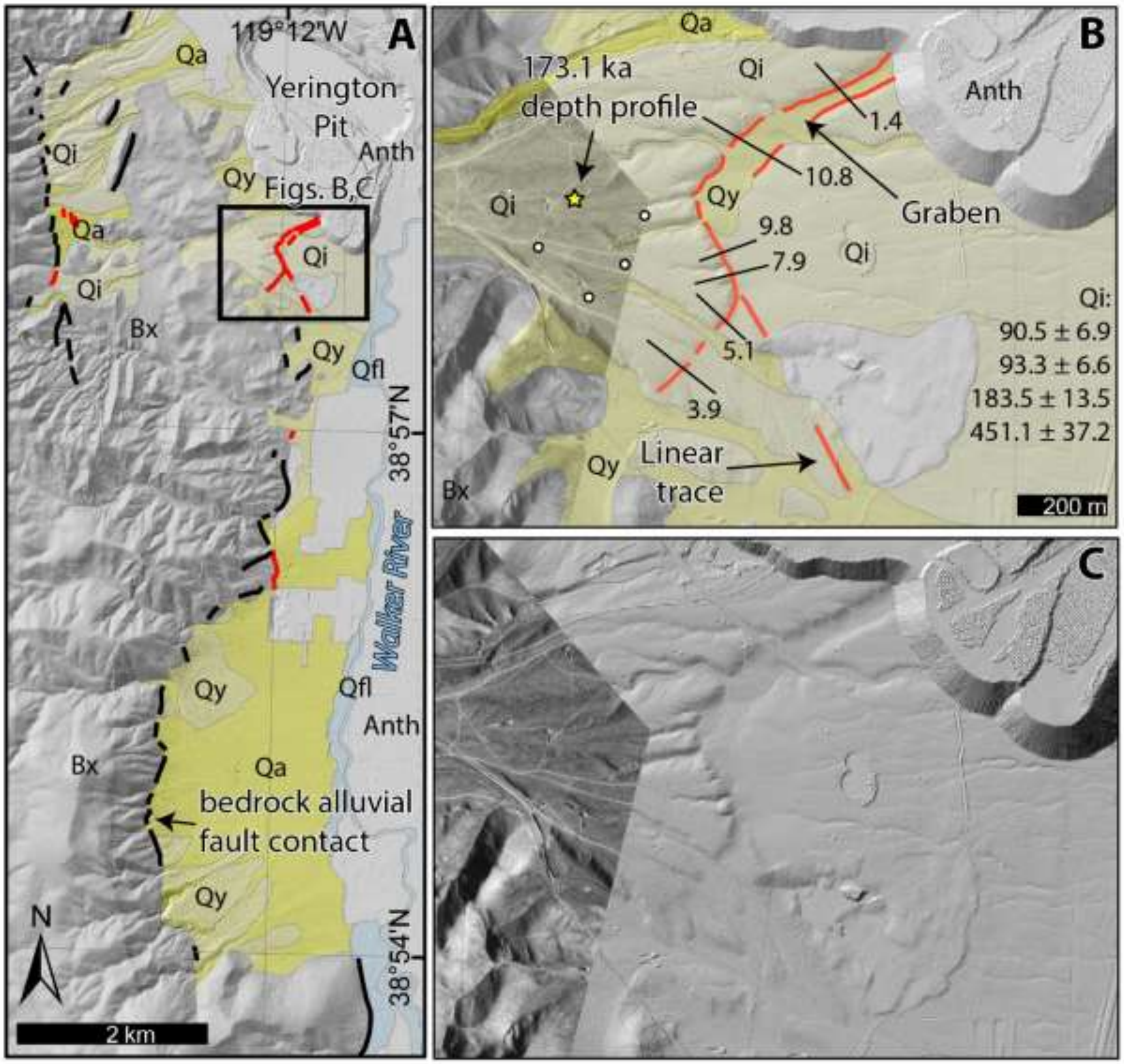

Figure 6 *Section of Mason Valley rangefront (a) showing lack of fault scarps preserved in alluvium (red) and location of Yerington fan slip rate site (b). Yerington fan rate site interpreted (b) and bare lidar hillshade / low sun angle aerial photo composite (c). Scarp profiles, heights (in m), and ages (ka) of boulder samples (white dots) are shown in (b), while the age and location of the depth profile (Figure 7) is indicated by the star.*

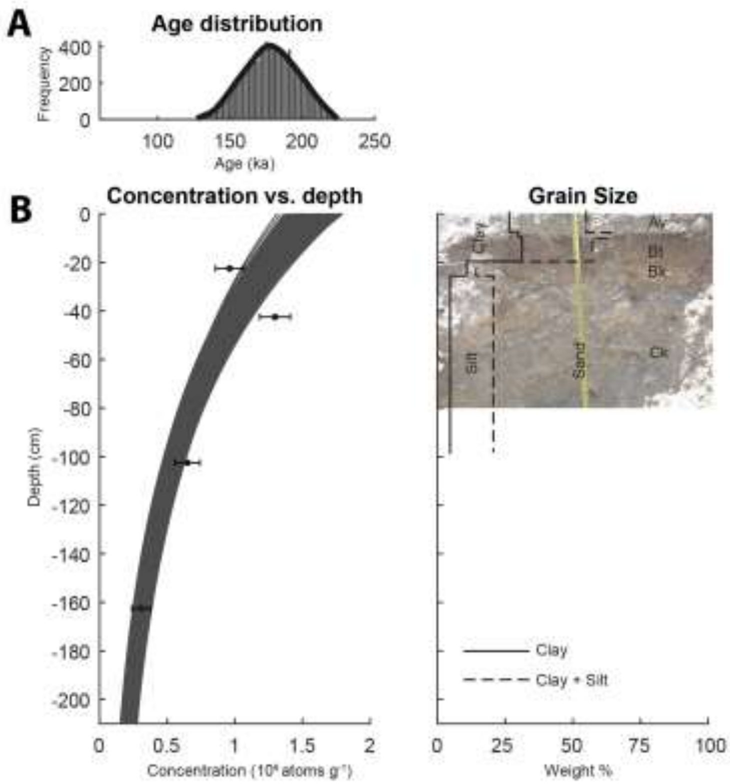

Figure 7 *Results for the Mason Valley depth profile sampled at the Yerington fan, modeled using the Hidy et al. (2010) MATLAB code. The resulting age is 173.1 $^{+38.7}/_{-32.5}$ ka. (a) distribution of modeled results for the age of the depth profile. (b) Monte Carlo solutions (left) of concentration of ^{10}Be vs. depth and soil textural analysis with well-developed Bt horizon (right) overlain on a photograph of the upper portion of the depth profile.*

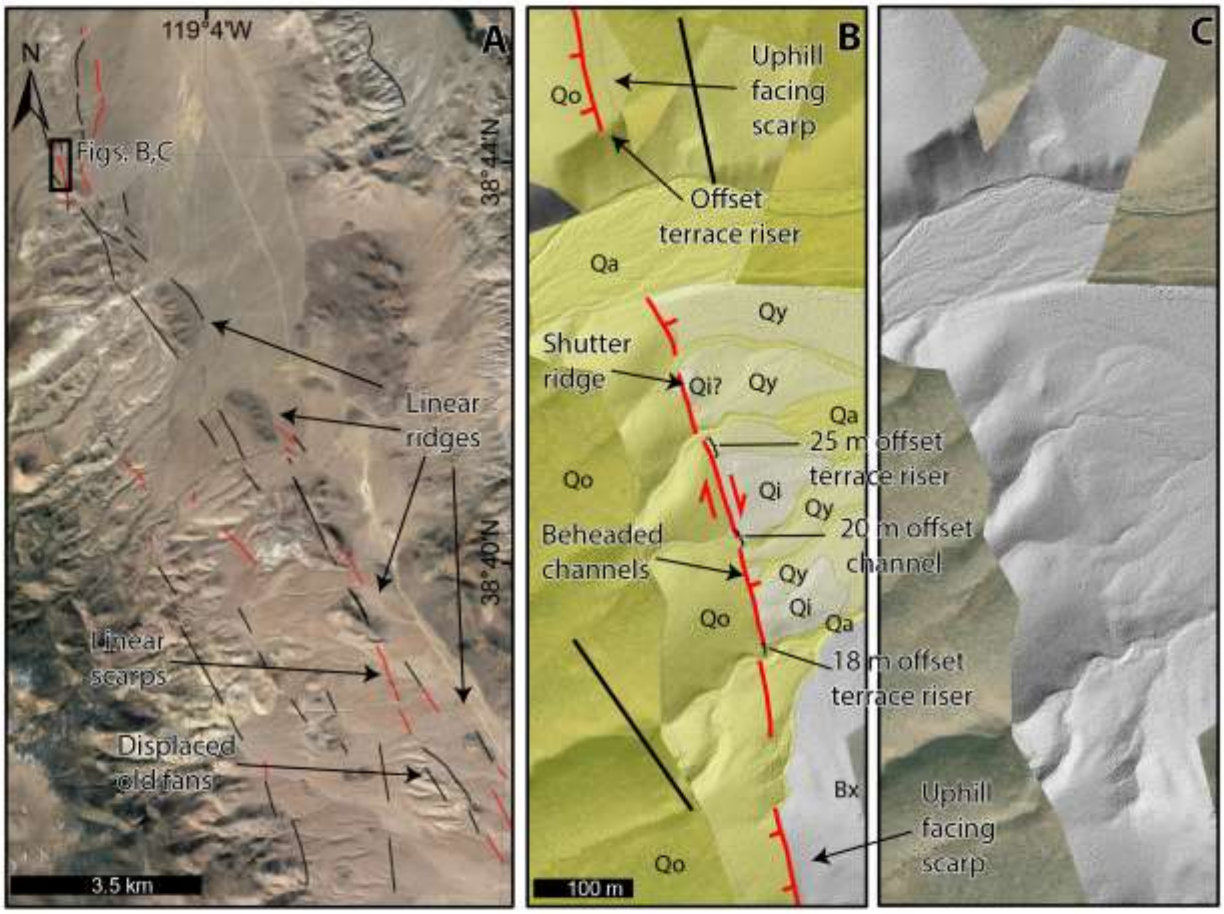

Figure 8 *Satellite image of the Pine Grove Hills fault zone in southern Mason Valley (a). Location indicated in Figure 2. Red lines indicate faults in alluvial deposits, while black are fault traces in bedrock. (b) shows an interpreted SfM model (c) of a section of this fault zone that demonstrates right-lateral displacements.*

3.4 Walker Lake Basin

The Walker Lake basin (**Figure 9**) is the largest basin of those examined and is ~100-km-long by 20-km-wide. The western margin of the basin is bound by the Wassuk range, which hosts a prominent active east-dipping normal fault, forming more than 2200 m of vertical relief. The vertical slip rate (>0.3–0.4 mm/yr) and paleoseismic history of this fault zone are described by Bormann et al. (2012). Dong et al. (2014) describe an active strike-slip fault in the northern part of the basin that displaces Lahontan aged shoreline deposits at a right-lateral slip rate of ~1 mm/yr (**Figure 9b**). Here observations are focused on additional evidence of strike-slip faulting and fault geometry (**Figure 9**).

The geometry of the Wassuk rangefront in **Figure 9a** provides a basis to divide the fault into 3 segments. From north to south, a linear northwest striking segment extending northwest from near Schurz, a central sinuous roughly north and northeast striking segment along the western shore of Walker Lake, and a southern northwest striking linear segment from Hawthorne to Whiskey Flat (**Figure 9d**). This central section forms a right-step in the fault system. The deepest portion of the basin, Walker Lake, is located in the right-step. This geometry of the

Walker Lake fault system has been previously described as a rhomboidal pull-apart in a strike-slip system (Mann, 2007), with Walker Lake itself situated in the depocenter of this pull-apart (Link et al., 1985). This geometry is similar to the step-over observed in Smith Valley, but on a larger scale (**Figures 2 and 4**).

Directly west of Hawthorne (**Figure 9c**) is a northwest-trending, linear, uphill-facing fault scarp that right laterally displaces two terrace risers as well as a series of gullies. From this area south to Lucky Boy Pass (**Figure 9d**), the fault forms a right-stepping pattern of north and northeast trending normal fault scarps and northwest trending linear scarps.

North of Lucky Boy pass are a series of north-striking grabens and prominent vertical fault scarps (**Figure 9d**). From Lucky Boy pass to the southeast is a linear northwest striking linear fault segment that extends for ~10 km. The first ~3 km of this fault segment forms a north facing fault scarp along the rangefront. The strike-slip fault trace then continues to the southeast linearly away from the rangefront forming subdued uphill-facing fault scarps. The remainder of this fault segment forms two fault traces that form south and north facing scarps and a prominent pop-up, pressure ridge-like feature of uplifted bedrock, fan, and pediment surfaces. South from here the fault bends to the southeast more and forms subdued scarps in a large distal fan, before again forming a second popup feature, similar in scale to the first. The rangefront southward from here is more northerly striking and forms a number of east facing scarps at canyon mouth drainages. The faulting mapped along a portion of the rangefront in **Figure 9d** is an example of strain partitioning: where a basin-ward strike-slip fault is separated from a rangefront normal fault.

The ~30-km-long series of fault segments extending from the southern margin of Walker Lake to Whiskey Flat (**Figure 9d**) is generally northwest striking. Normal displacements observed in north-striking bends are systematically larger than observed along the northwest-striking linear segments. The linearity of the fault traces, the alternating-facing fault scarps, and the several beheaded channels and lateral displacements in the northwest-striking portions of the fault zone, and the magnitude of scarps in the north-striking right-steps are all consistent with northwest directed dextral faulting.

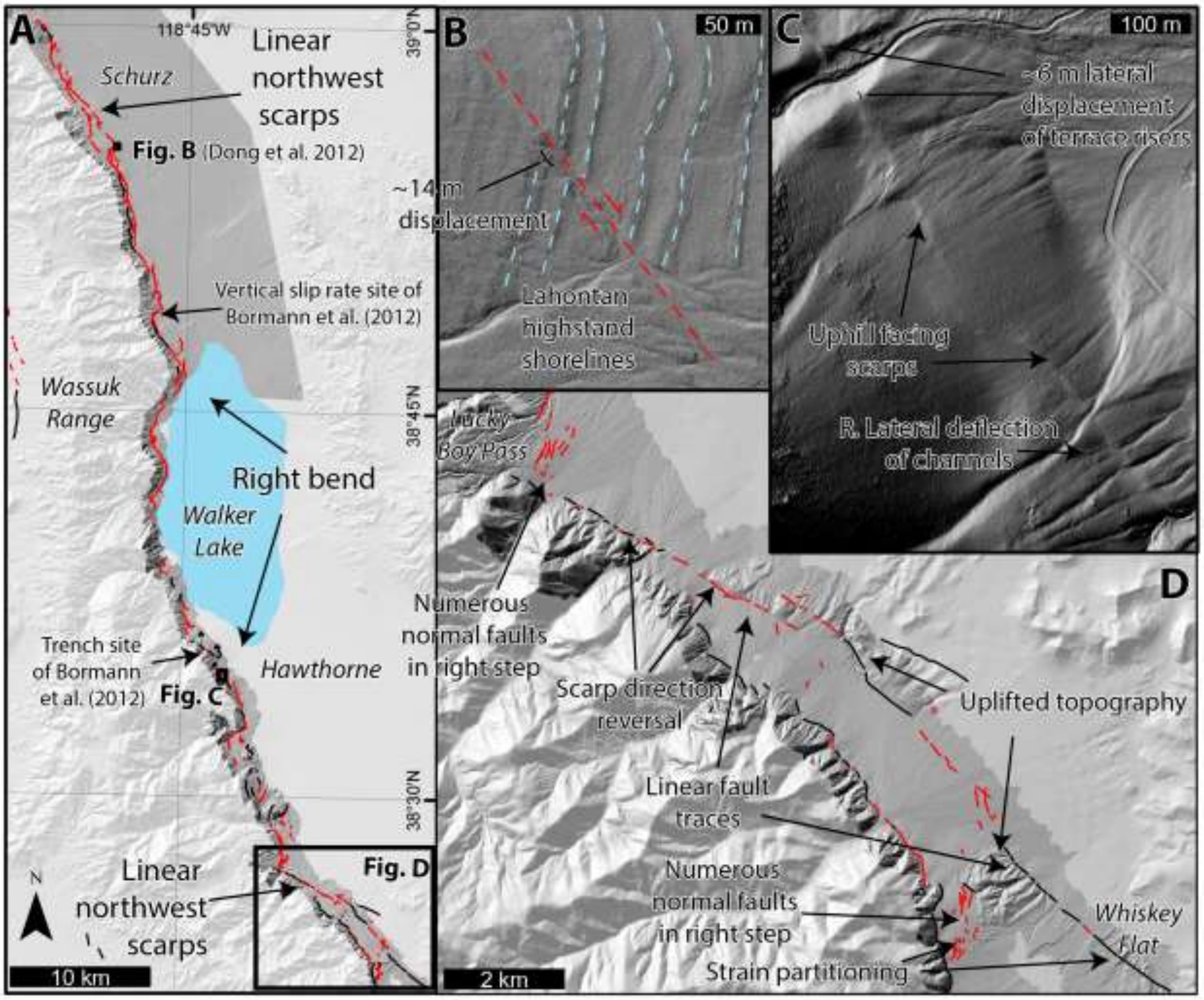

Figure 9 *Fault map (a) of the Wassuk fault zone. Lidar hillshades are darker gray, light gray background is a hillshaded 10 m DEM. Red lines are fault scarps in alluvial deposits, black are inferred and/or bedrock-alluvial fault contacts. The fault geometry forms two northwest striking segments separated by a large right step coincident with Walker Lake and the deepest part of the basin. The northwest striking segments contain alternating scarp directions, linear scarps, and right-lateral displacements, all consistent with strike-slip faulting. Right-stepping segments locally exhibit greater degrees of normal faulting. Locations of (b-d) are indicated on (a). (b) Blowup of site from Dong et al. (2014) showing 14 m right-lateral displacement of ~14.5 ka Lahontan shorelines with slip rate of ~1 mm/yr. (c) Segment of fault near Hawthorne where an uphill facing linear scarp deflects a number of channels and offsets a pair of terrace risers ~6 m. (d) shows the southern portion of the Wassuk fault zone. Here strain is partitioned into a linear basin-ward strike-slip fault and a normal fault against the range.*

4 Discussion

4.1 Displacement distributions, recurrence intervals, expected magnitudes of earthquakes, and "short" faults in the Central Walker Lane

Scarp heights are measured along the lengths of the Smith and Antelope valley rangefront faults to produce displacement distribution plots (**Figures 2 and 10**). These scarp heights are snapped to a linear approximation of each rangefront fault. The distance along this line of each of these measurements is plotted against the height of each measurement to demonstrate the distribution of scarp heights along the strike of the fault. Additionally, histograms with 1.0 m vertical displacement bins are presented to analyze the displacement distribution for clusters that might be attributable to individual paleoseismic events (**Figure 10**). Combining these displacement distribution plots (**Figure 10)** with the length of the faults and the slip rates (**Figure 4)** for the range-bounding faults in Smith and Antelope valleys allows for an estimation of the magnitude of paleoearthquakes as well as anticipated average return times for earthquakes.

The most recent two peaks of the histograms of vertical displacements for Antelope and Smith valleys (**Figure 10**) are interpreted as the vertical displacement resulting from the most recent event (MRE) and penultimate earthquakes. These displacements are 3.9 and 2.1 m for Smith Valley and 3.2 and 3 m for Antelope Valley. Displacements observed in prior paleoseismic trench studies on the two faults are similar: 3.5 m for the MRE in Smith Valley (Wesnousky and Caffee, 2011) and 3.6 and 2 m (Sarmiento et al., 2011) for the MRE and penultimate earthquakes in Antelope Valley.

For Smith Valley, dividing the 3.9 and 2.1 m MRE and penultimate events by the ~0.6 mm/yr vertical separation rate determined for the fault in this study results in estimated earthquake return times ranging from 3500 to 6500 years. The result is in general accord with the report of the single earthquake ~3000 years ago reported by the paleoseismic trench study of Wesnousky and Caffee (2011) for the fault. For Antelope Valley, dividing the 3.2 and 3 m displacements by the 0.5 mm/yr vertical separation rate results in earthquake return times ranging from 6000 to 6400 years. Sarmiento et al.'s (2011) trenching study in Antelope Valley showed an inter-event time between the most recent and penultimate earthquakes equal to ~5000 years, which is also similar to the ~6000 year estimate based on the slip rate and displacement distribution.

The definition of moment magnitude is (modified after Hanks and Kanamori, 1979):

$$M_w = \frac{2}{3}\log(\mu A d) - 10.7$$

where, here we assume that the fault area (*A*) is equivalent to the fault width (15 km estimated here) multiplied by the measured map view length of each fault (50- and 22-km for Smith and Antelope valleys, respectively), the average displacement (*d*) is measured for the MRE from the displacement distributions, and the shear modulus (μ) is 3 x 10^{11} dynes/cm^2. These inputs result in an expected M_w 7.3 for Smith Valley and M_w 7.0 for Antelope Valley for the most recent events on each fault, respectively. Surficial displacements are less than fault displacement at depth, and fault rupture lengths are poorly constrained by mapped fault scarps, so these are likely underestimates of magnitude.

Using the relation of fault length to moment magnitude from Wesnousky (2008) results in expected magnitudes of 6.9 and 6.7 for the 50- and 22-km-long faults in Smith and Antelope valleys, respectively. These estimates are approximately a quarter magnitude less than estimated using the moment magnitude equation above. Likewise, for the mapped fault lengths, the expected displacements for these faults should be on average 1.5 and 0.7 m, with maxima of 4.5 and 2.0 m, respectively (Wesnousky, 2008). These average values are roughly half and a quarter of what is observed along the Smith and Antelope valley rangefront faults, respectively. Average displacements of ~3 m, similar to values observed on each of these faults, are typically associated with a normal fault surface rupture length of ~100 km (Wesnousky, 2008). Two hypotheses can explain the observation that observed fault lengths appear insufficient to produce the observed offsets: (1) faults in this part of the Walker Lane rupture with other nearby faults producing longer total rupture lengths, or (2) these faults rupture independently and produce high-stress drop earthquakes.

The size of the observed single event displacements on a number of other faults in this region (e.g., the Incline Village, Little Valley, Stateline, Pine Grove Hills, Bridgeport Valley, and the unnamed faults of eastern Mason Valley) are also greater than expected from historical observations relating fault rupture length to displacement (Wesnousky, 2008; Seitz and Kent, 2014). The traces of several of these faults are less than 20 km yet some have been demonstrated to have produced single event displacements of ~3 m. Faults in the Central Walker Lane may produce complicated, multi-segment ruptures with multiple shorter fault strands (including previously unrecognized fault strands) supporting larger (M_w 7+) earthquakes, not dissimilar to the 1891 M_w 7.5 Nobi, Japan (Kaneda and Okada, 2008), 1932 M_s7.2 Cedar Mountain, Nevada (Bell et al., 1999), 1970 M_s 7.2 Gediz, Turkey (Ambraseys and Tchalenko, 1972), or 2016 M_w 7.8 Kaikoura, New Zealand (Hamling et al., 2017) earthquakes. In Smith Valley, for example, the rangefront fault may produce ruptures extending further south along strike towards Strawberry Flat, or even as far as Bridgeport Valley, where numerous large normal fault scarps are preserved in these two small (~15-km-long) basins (**Figure 11a**). This would result in a total rupture length of ~75-100 km, as one might expect based on the measured displacements and the relations in Wesnousky (2008). Antelope Valley might rupture along with faults to the north in the East Carson Valley fault zone, increasing rupture length from ~20 to ~65 km (**Figure 11a**).

It is also possible that the earthquake ruptures in this region are indeed limited to these short mapped fault traces, as normal faults have historically produced large displacements with short rupture lengths in the Basin and Range (e.g. the 1959 M_w 7.2 Hebgen Lake earthquake produced an average displacement of 2.9 m over a 27-km-long rupture; Myers and Hamilton, 1964). If fault ruptures in this part of the Walker Lane are indeed “short”, then to produce the same displacements as earthquakes with typically longer ruptures implies that these earthquakes have a high stress-drop. Hecker et al. (2010) show that faults with low slip rates and little cumulative slip, like those in the Central Walker Lane, produce particularly high static stress-drop earthquakes. Perhaps this is evidence that faults in this part of the Walker Lane are stronger than faults elsewhere in the Cordillera, which is counterintuitive to what one might expect based on the high geothermal gradient and shallow crust of this region.

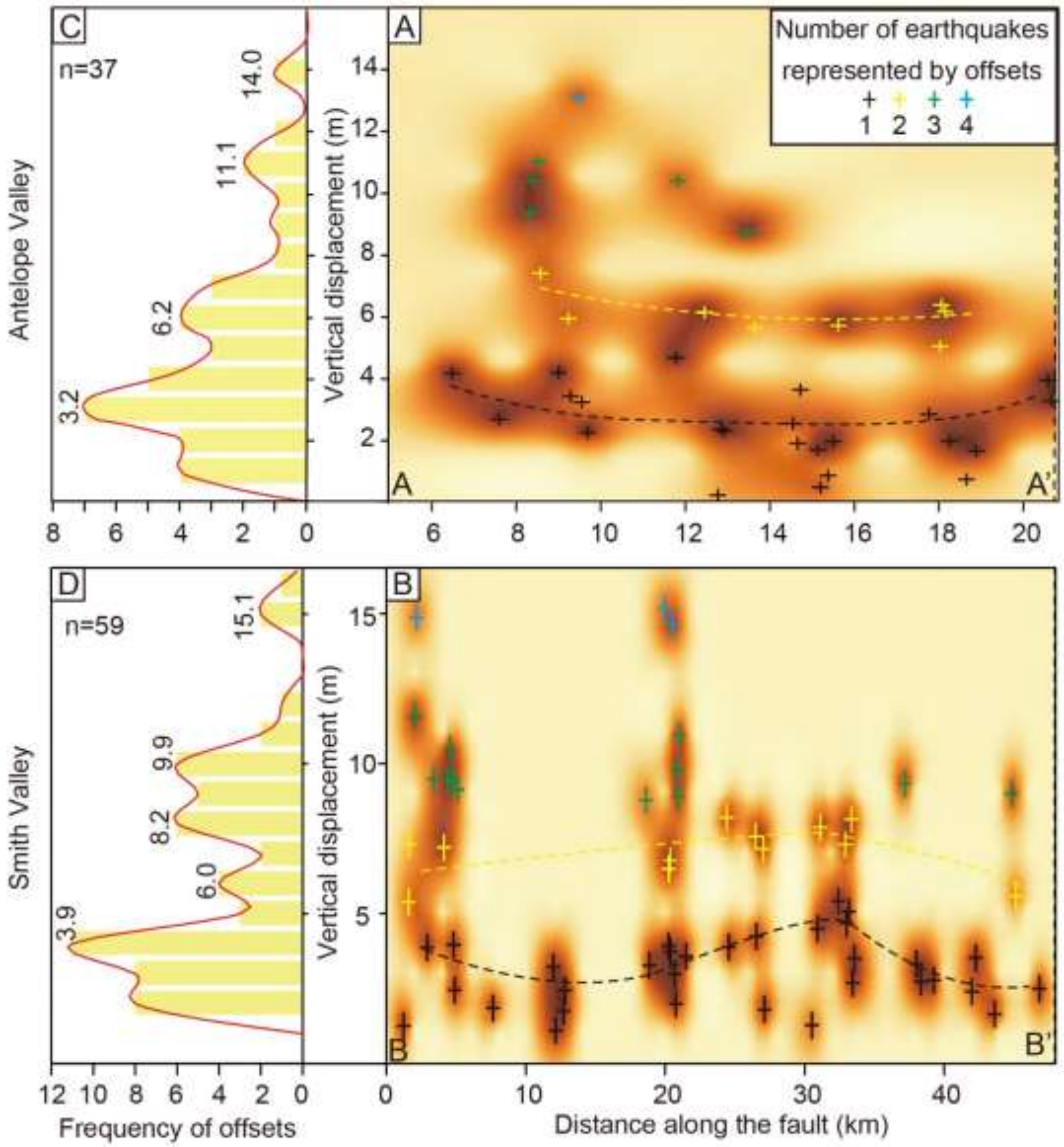

Figure 10 Slip distribution plots (a, b) and displacement histograms (c, d) for Antelope Valley (a, c) and Smith Valley (b, d). Locations of cross sections indicated on Figure 2. The displacement of the most recent and penultimate earthquakes for each fault can be estimated by looking at the smallest two peaks of each histogram. For the slip distributions (a, b), darker colors indicate higher probabilities. The colored crosses represent our interpretation of the number of earthquakes which produced each displacement measurement.

4.2 Geodetic vs. geologic rates and off-fault deformation in the Central Walker Lane

In this paper two different methods of estimating geodetic shear are compared to geologic slip rates. The first geodetic method measures the total geodetically observed shear in a profile across a region (**Figure 12a**), and the second method uses the individual slip rates assigned to faults by a block model (**Table 2**). **Figure 12a** is a compilation of our dextral slip rate estimates and published geologic right-lateral slip rates across the Walker Lane (small numbers), compared to profiles of geodetic rates (rectangles) measured across the entire Walker Lane (modified after Bormann in Redwine et al., 2015). The percentages are the ratio of the sum of the geologic strike-slip rates of all of the known faults (first large number) to the total shear across a profile measured geodetically (second large number). The ratio can be thought of as the kinematic efficiency as defined by Hatem et al. 2017 and directly compared to the results of laboratory studies.

Geodetic block models generally only consider the horizontal component of the GPS velocity when solving for fault slip rates, and are therefore most reliable for measuring the horizontal strike-slip and extensional (or compressional) slip rates. Thus, an assumption of fault dip must be made to directly compare geodetic rates to the vertical separation rates measured in this study. To calculate the extensional components and down-dip slip rates of the range bounding faults in Mason, Smith, and Antelope valleys we assume that they have a simple normal fault geometry with a dip of 55 ± 10°.

The vertical separation rates and resulting extension and dip-parallel slip rates for the Walker Lake and Mason, Smith, and Antelope valley range-bounding faults are listed in **Table 2** along with the block modeled rates for the same faults from Bormann et al. (2016). The geologic and geodetic extension rates for the Wassuks and Smith and Antelope valleys are very similar. The block modeled right-lateral rate for the Wassuk range is ~0.6 mm/yr which is similar to the geologic rate of ~1 mm/yr (Dong et al., 2014). However, the geodetic right lateral strike-slip rate of 1.1 ± 0.4 mm/yr in Antelope Valley is among the fastest rates in the region, yet lacks any observable geomorphic expression of strike-slip. The small faults on the east side of Antelope Valley with right-lateral displacements do not appear sufficiently active to account for this rate. The normal slip rate estimate in Antelope Valley of $0.6\ ^{+0.6}/_{-0.4}$ mm/yr is similar to the 0.7 mm/yr estimate that Sarmiento et al. (2011) made based on the displacement measured in their trench and the inter-event time. The extension rate in Antelope Valley of $0.4\ ^{+0.4}/_{-0.2}$ is slightly less but similar to the block model rate of 0.7 ± 0.5 mm/yr (Bormann et al., 2016).

In Smith Valley, the GPS block model predicts ~0.4 mm/yr of extension and ~0.5 mm/yr of right-lateral strike-slip (Bormann et al., 2016). The geologic extension rate measured at the Artesia fan is ~0.4 mm/yr (**Table 2**), similar to this geodetic estimate. As this rate was measured on the edge of a large right-bend that is nearly perpendicular to the overall trend of the rangefront fault (**Figure 5**), this extension rate may be directly recording the lateral component of motion along the fault. Furthermore, the overall Smith Valley rangefront is much less sinuous than many normal faults in the region (**Figure 11**), suggesting it accommodates lateral slip.

In Mason Valley, the geologic rates of <0.05 mm/yr are an order of magnitude less than the geodetic estimate of ~0.5 mm/yr, and while the fault geometry at the Yerington Pit site allows for the accommodation of right-lateral slip, the measured geologic slip rates are close to zero. As the Singatse Range is much more subdued in topographic expression than other ranges in this region, and the rangefront generally lacks the uplifted, faulted fan surfaces common to the other faults in the region with slip rates of ~0.5 mm/yr, it seems possible that the geodetic models have not correctly partitioned the amount of slip on faults across the region, and that the much lower geologic rate seems more likely. In contrast, the fault morphology observed between the Pine Grove Hills and the southernmost part of Mason Valley appears sufficiently developed to satisfy the geodetically predicted slip rate of ~0.6 ± 0.5 mm/yr, despite any age control on displaced surfaces.

The discrepancies between geologic and geodetic slip rates in Mason and Antelope valleys may be a result of the limitations of the block model. Block models assume that all of the deformation between two adjacent blocks is constrained to a singular fault trace, which is often the only trace measurable using paleoseismic methods. However, laboratory shear models of fault systems with discontinuous geometries similar to the Walker Lane accommodate a significant portion of their total shear strain through diffused, off-fault deformation in the intervening regions between and around well-defined faults (e.g., Hatem et al., 2017), which cannot be accurately modeled as boundaries between rigid blocks. The laboratory models of Hatem et al. (2017) show that even mature through-going fault systems are only ~80% efficient, with ~20% of total shear accommodated by off-fault deformation, while immature systems like the Walker Lane can be less than 40% efficient, with >60% of the total shear accommodated off of faults. In the Walker Lane kinematic efficiencies vary from as little as 35% in the Central Walker Lane to ~100% in the Southern Walker Lane (**Figure 12a**). In this perspective, it may be speculated that the geologic slip rates in the Southern Walker Lane may be overestimated, as they do not leave any of the shear budget for off-fault deformation.

Geologically accounting for this off-fault coseismic deformation generally requires detailed pre- and post-earthquake observations of a fault system, and is therefore difficult to account for in the paleoseismic record by measuring multiple-event fault scarps (e.g., Oskin et al., 2012; Herbert et al., 2014; Gold et al., 2015; Personius et al., 2017). This deformation may manifest in different ways for each earthquake, or may be sufficiently limited in scale or diffuse that it is unlikely to be preserved on the landscape over multiple earthquake cycles. Furthermore, the orientation of some of the normal faults in the western Central Walker Lane allow for the accommodation of some of the regional shear. Thus, while only ~35% of the total shear across the Central Walker Lane is currently accounted for by summing the slip rates of known strike-slip and oblique faults, and some “on-fault” shear may still be missing, it does not appear that the sum of the lateral slip rates of the individual faults must necessarily equal the total geodetic shear across a fault system, and that both distributed shear and complex fault relationships can accommodate a significant portion of “off-fault” shear, especially in immature systems such as the Walker Lane.

Many studies of faults in the Walker Lane have shown evidence of significant temporal and spatial variations in fault geometries, slip rates, and styles of faulting (e.g., Kirby et al., 2006; Frankel et al., 2007; Gourmelen et al., 2011; Gold et al., 2013; Rittase et al., 2014). Geodetic rates are measured on a decadal timescale, whereas most geologic slip rates are over 10^4–10^5 year time scales, and if slip rates have fluctuated with time, the geodetic rates may not be representative of longer term crustal deformation. At the current ~7-8 mm/yr rate of dextral crustal shear across the Central Walker Lane, it would have taken ~4 Ma to accumulate the estimated ~30 km of total shear. This estimate fits with geologic estimates on the timing of the initiation of shear in the Northern Walker Lane occurring between 10 and 3 Ma (Faulds and Henry, 2008), and is likely a young estimate if the rate of shear has accelerated since initiation.

Few studies of geologic slip rates on timescales longer than 10^5 years have been conducted in this region, but Surpless and Kroeger (2015) show that for the Wassuk Range, slip rates have been fairly constant since ~4 Ma, are similar to the geodetic estimates, and thus decadal scale modern geodetic rates may be an accurate measure of longer term deformation in this region. As most of the block-modeled geodetic rates are in general accord with the geologic slip rates presented here, it may be suggested that the slip rates of the faults studied have been relatively constant over the Late Quaternary.

Table 2. Slip Rates from this study compared to block modeled rates from Bormann et al. (2016).

TABLE 2. SLIP RATES

	Vertical	Dip Parallel (55± 10° normal fault)	Extension	Strike-Slip	GPS Extension[a]	GPS Strike-Slip[a]
Artesia Qy	0.5 +0.7/-0.2	0.6 + 0.9/-0.2	0.4 +0.5/-0.1	0.4?	0.4 ± 0.5	0.5 ± 0.4
Artesia Qi	0.6 +0.8/-0.4	0.7 + 1.0/-0.5	0.4 +0.6/-0.3	0.4?	0.4 ± 0.5	0.5 ± 0.4
Antelope Valley	0.5 +0.5/-0.3	0.6 + 0.6/-0.4	0.4 +0.4/-0.2	-	0.7 ± 0.5	1.1 ± 0.4
Mason Valley (Singatse)	0.05 ± 0.01	0.06 ± 0.01	0.04 ± 0.01	-	0.6 ± 0.5	0.4 ± 0.4
Pine Grove Hills	-	-	-	-	0.2 ± 0.6	0.6 ± 0.5
Wassuk/Walker Lake	0.8 ± 0.2[b]	-	-	1.0[c]	0.7 ± 0.3	0.6 ± 0.4

[a]from Bormann et al. (2016)
[b]from Surpless and Kroeger (2015)
[c]from Dong et al. (2014)

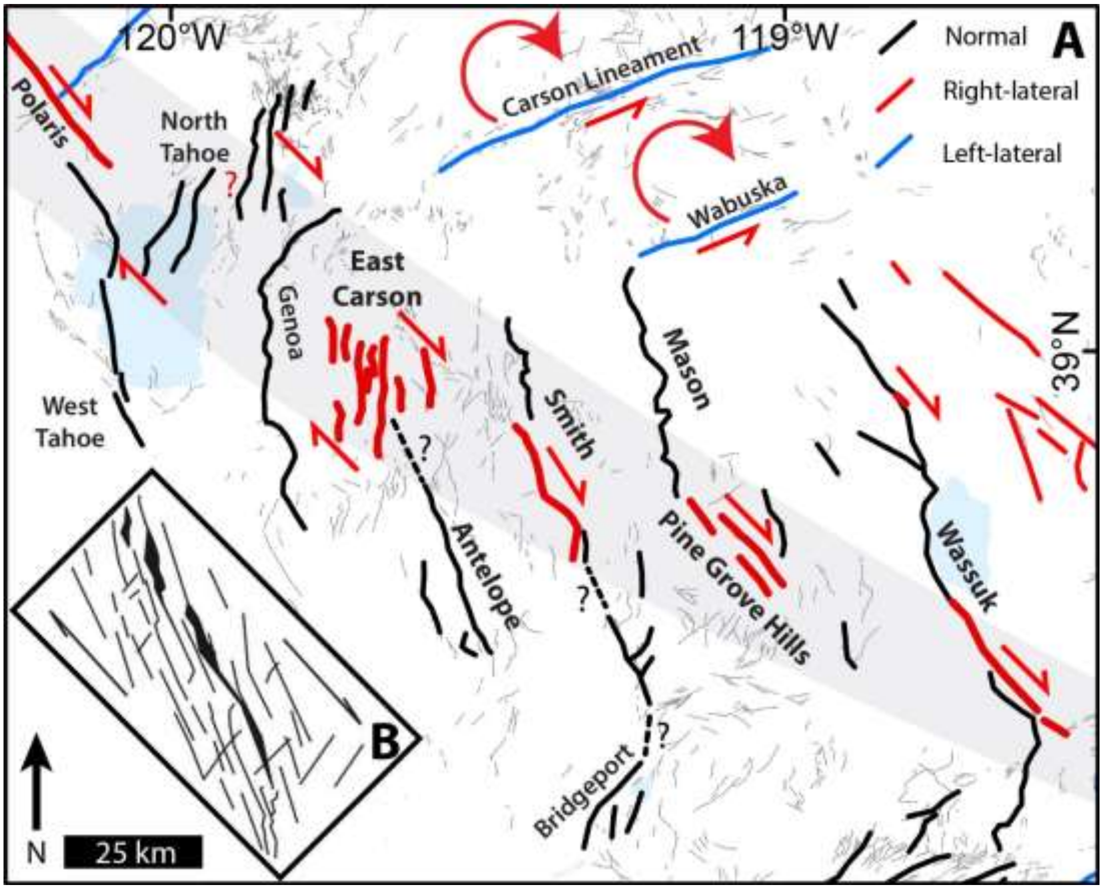

Figure 11 *(a) Fault pattern of the Central Walker Lane. The grey band demonstrates a well-defined zone of en-echelon left-stepping dextral strike-slip faulting. Queried dashed lines indicate possible connections between faults as discussed in text. (b) Sketch of a clay model copied from Atmaoui et al. (2006) produces a similar pattern of left stepping en echelon faults and basins as is observed in the Central Walker Lane.*

4.3 On the lack of strike-slip in the Central Walker Lane

A paleomagnetic survey of the region completed by Carlson (2017) suggests that little rotation has occurred between Antelope, Smith, and Mason valleys, while considerable rotations have accumulated in the Carson domain. The lack of rotation between Antelope and Mason valleys is further supported by the displacement distribution plots in **Figure 10**: if mountain ranges were actively rotating in a clockwise direction, and this rotation were accommodated by the rangefront faults, it might be expected that slip during earthquakes along the ranges would be distributed such that the largest displacements would occur near the northernmost or southernmost parts of the ranges with lesser displacements in the central portions. Repeated earthquakes with this distribution would result in greater structural relief at the northern and southern parts of ranges, but neither of these patterns are observed, and instead displacement distributions are relatively uniform with the highest relief being generally near the central portions of ranges. Strike-slip faulting should therefore accommodate any shear between these basins in the absence of significant rotations.

Well defined active strike-slip faults are observed in the Walker Lake basin (e.g. Dong et al., 2014), Truckee basin (Polaris fault; Hunter et al., 2011) and in the southern part of Mason Valley (**Figure 11a**). Despite the absence of discrete measurable offsets, the geometry of the Smith Valley range front fault allows that the rangefront fault accommodates a significant portion of right-lateral shear (**Figure 5**). DePolo and Sawyer (2005) report observing strike-slip faulting in the East Carson Valley fault zone (**Figure 11a**), though the rate of slip across this broad and complex zone of discontinuous faults remains undefined. The short, northeast-striking faults of the North Tahoe fault system (labeled North Tahoe in **Figure 11a**, including the Stateline, Incline Village, Little Valley, and Washoe Valley faults) form an en-echelon right stepping pattern (**Figure 11a**) and may be considered book-shelf faults (e.g., Tapponnier et al., 1990), accommodating northwest-directed dextral shear. Thus, while slip rate indicators are not consistently preserved or recognized along all rangefronts and adjacent valleys, the geometry and pattern of faulting along with the distribution of late Quaternary slip as a function of fault strike indicates that there is a significantly larger portion of shear being accommodated by active strike-slip fault displacements than we have yet been able to quantify.

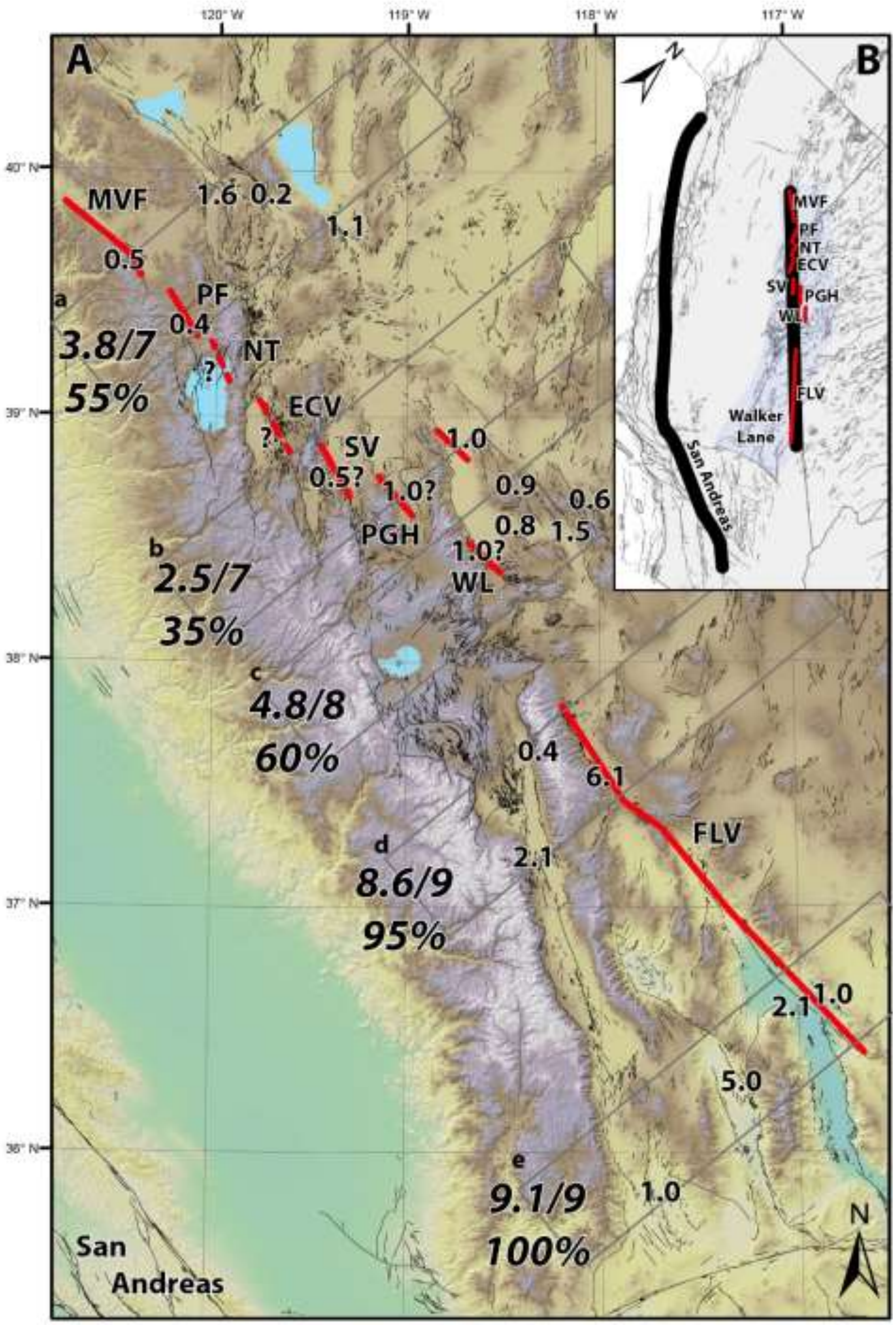

Figure 12

Figure 12. (a) Comparison of dextral shear rates measured across the Walker Lane in various profiles (gray boxes) by GPS (bold numbers), and on individual faults (smaller numbers), in mm/yr (fault slip rates from: Kirby et al., 2006; Guest et al., 2007; Frankel et al., 2011; Hunter et al., 2011; Amos et al., 2013; Gold Ryan D. et al., 2013; Dong et al., 2014; Gold et al., 2014; Angster et al., 2016; Choi, 2016; Frankel et al., 2016; Haddon et al., 2016; Gold et al., 2017). These GPS rates were provided by J. Bormann and are contained in Redwine et al. (2015). The percentages are taken by summing the rates of individual faults in each profile and dividing those by the total geodetic rate in each profile. There is good agreement between geodetic and geologic observations in the Southern Walker Lane, but less so in the Central and Northern Walker Lane. Major strike-slip fault zone discussed in this paper is highlighted by bold red lines with fault abbreviations: FLV-Fish Lake Valley, WL-Walker Lake, PGH-Pine Grove Hills, SV-Smith Valley, ECV-East Carson Valley, NT-North Tahoe, PF- Polaris Fault, MVF-Mohawk Valley. (b) Oblique oriented map of California and Nevada showing the trend of these faults as a bold black line (right) that is subparallel to the San Andreas (left black line).

4.4 Geometry of an incipient strike-slip system

The grey band in **Figure 11a** highlights the series of fault systems described in the preceding section. Each of these six fault systems is ~25-km-long, and is separated from its neighboring strike-slip faults by left steps ranging in size from ~15 to 25 km. Together these fault systems form a clear en-echelon left-stepping ~25-km-wide pattern of active dextral faults extending for ~200 km from south of Walker Lake to north of Lake Tahoe.

The pattern of faults presented in **Figure 11a** is consistent with the early stages of models of distributed strike-slip fault systems (e.g., Schreurs, 2003; Hatem et al., 2017) such as shown in **Figure 11b**. This model produces a discontinuous pattern of left-stepping Riedel shears that form en-echelon extensional basins and dextral faults similar to what is observed in the Central Walker Lane (Atmaoui et al., 2006). All of the faults in these models begin as extensional cracks. Aydin and Nur (1982) show that pull-apart basins in a strike-slip system are largely a result of step overs of en-echelon strike-slip faults, which is consistent with the pattern of faulting observed in the Central Walker Lane. Thus, the majority of north-striking normal faulting along a number of the ranges in this region is driven by northwest directed dextral shear along discrete faults, similar to these experimental models (e.g., Aydin and Nur, 1982; Atmaoui et al., 2006). In this light the westward decrease in inception age and total magnitude of extension and normal faulting from the Wassuk Range to the Sierra Nevada may be evidence for the encroachment of strike-slip faulting through this region.

When viewed in large scale the pattern of strike-slip faulting in the Central Walker Lane falls on strike with both the Mohawk Valley and the Death Valley/Fish Lake Valley faults (**Figures 1, 12**), which are among the most active strike-slip faults of the Northern and Southern Walker Lane, respectively. Laboratory models predict that as displacement accumulates across fault systems, initial distributed faulting will eventually organize into a single through going strike-slip fault. The trend of faults illustrated by the right bold line in **Figure 12b** forms a linear, >500-km-long fault zone that is nearly parallel to the San Andreas fault, and eventually this may be the trace of a continuous strike-slip fault, accommodating much of the strain across the Pacific-North American plate boundary. However, fault complexity is not solely a result of total shear accumulated across a fault zone, as faults largely take advantage of pre-existing crustal weaknesses (e.g., Molnar, 1988; Ziegler et al., 1998; Matenco et al., 2007; Dyksterhuis and Müller, 2008; Aitken et al., 2013; Raimondo et al., 2014; Calzolari et al., 2016), which in the Walker Lane may have been inherited from an earlier episode of Basin and Range extension, prior to initiation of the current Walker Lane strain regime (Surpless et al., 2002), or even earlier structural irregularities (e.g. Faulds and Henry, 2008).

The nuances in the structural evolution of transtensional systems are highlighted here by two other transtensional fault systems that are analogous to the Walker Lane: the Shanxi Rift system of China, and the Aegean-West Anatolian extensional province of Turkey (**Figure 13**). The Shanxi Rift forms a ~650-km-long by 100-km-wide zone of discontinuous northeast trending normal and strike-slip faults, where the relatively stable Ordos block is moving obliquely relative to the North China plain (**Figure 13b**) at a current relative geodetic rate of ~2 mm/yr (Zhao et al., 2017). While the Shanxi Rift has only accumulated ~10 km of total shear (Xu et al., 1993), much less than the Walker Lane, these two systems have similar fault patterns of discontinuous, en-echelon strike-slip and normal faults. The Aegean-West Anatolian extensional province (**Figure 13c**) of Turkey is a complex series of strike-slip and normal faults extending to the south of the North Anatolia fault (e.g. Faulds et al., 2009). A north-south oriented GPS profile across this province shows that ~5-10 mm/yr of east-directed dextral shear and ~20 mm/yr of north-direct extension is accommodated over a width of ~300 km (Figure 9b in Aktug et al., 2009). Although we are unaware of any estimates of cumulative shear across this broad province, and the rate of extension is an order of magnitude higher than the Walker Lane, the pattern of faulting and rate of distributed shear in this province are both analogous to the Walker Lane (**Figure 13**). Total cumulative slip in all three of these systems is limited, and the transtension accommodated by each system forms a similar pattern of broad, complex, discontinuous faulting.

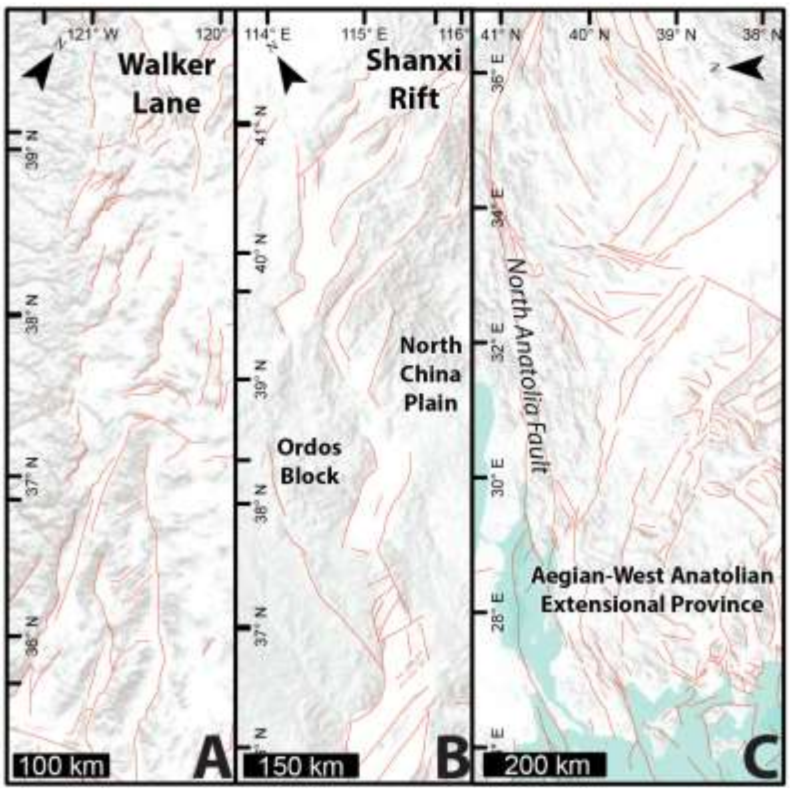

Figure 13 *Fault pattern of the Walker Lane (a) compared to the Shanxi Rift of China (b) and the Aegian-West Anatolian Extensional Province of Turkey (c). All maps are oriented so that the major dextral shear directions are subparallel.*

5 Conclusions

- Slip rates of normal faulting for the Antelope, Smith, and Mason valley rangefront faults are 0.6 $^{+0.7}/_{-0.3}$, 0.7 $^{+1.0}/_{-0.4}$, and <0.05 mm/yr, respectively.
- Preservation of geomorphic features indicating strike-slip faulting are lacking along the Antelope and Mason valley rangefront faults.
- A large component of strike slip is indicated along the Smith Valley fault by a correlation of scarp size and preservation to variations in fault strike.
- Scarp height distributions measured from lidar along the Smith and Antelope valley range bounding faults agree well with observations from previous paleoseismic trenches, with single event displacements of ~3 m for both faults that correspond with earthquakes of ~M_w 7.
- Discrete strike-slip faults previously unrecognized are described in the southern parts of Mason Valley and the Walker Lake basin.
- Significant geodetically observed shear remains unaccounted for by summing geologic slip rates, but is likely accommodated by off-fault deformation and complex rupture patterns.
- Shear in the western part of the Central Walker Lane is accommodated along a system of short, left-stepping en-echelon dextral and normal faults extending from south of Walker Lake to north of Lake Tahoe. Together this system of faults forms a pattern similar to the initial stages of laboratory models of dextral shear, and may evolve into a through-going strike-slip fault in the future.

Acknowledgements

This research was supported in part by National Science Foundation grant EAR-1419724 and EAR-1419789 and by USGS grant G15AP00088. Any use of trade, firm, or product names is for descriptive purposes only and does not imply endorsement. We thank Paula Figueiredo and Sarah Hammer for assistance in processing and calculating TCN ages, and the National Center for Airborne Laser Mapping (NCALM) for collecting lidar data (available at opentopography.org). Thanks to Steve Angster, Tabor Reedy, Chad Carlson, Noah Abramson, Annie Kell, Colin Chupik, Jayne Bormann, Bill Hammond, Ken Adams, and Rachel Hatch for assisting in the field, lab, and numerous enlightening discussions. Thanks to the 2017 UNR Neotectonics class for assistance in the field. Thanks to Rich Koehler for editing an early version of this manuscript. This is Center for Neotectonic Studies contribution number 78.

References

Adams, K.D., Wesnousky, S.G., 1998. Shoreline processes and the age of the Lake Lahontan highstand in the Jessup embayment, Nevada. Geol. Soc. Am. Bull. 110, 1318–1332.

Aitken, A.R.A., Raimondo, T., Capitanio, F.A., 2013. The intraplate character of supercontinent tectonics. Gondwana Res. 24, 807–814. https://doi.org/10.1016/j.gr.2013.03.005

Aktug, B., Nocquet, J.M., Cingöz, A., Parsons, B., Erkan, Y., England, P., Lenk, O., Gürdal, M.A., Kilicoglu, A., Akdeniz, H., Tekgül, A., 2009. Deformation of western Turkey from a combination of permanent and campaign GPS data: Limits to block-like behavior. J. Geophys. Res. Solid Earth 114. https://doi.org/10.1029/2008JB006000

Ambraseys, N.N., Tchalenko, J.S., 1972. Seismotectonic Aspects of the Gediz, Turkey, Earthquake of March 1970. Geophys. J. R. Astron. Soc. 30, 229–252. https://doi.org/10.1111/j.1365-246X.1972.tb05811.x

An, L.-J., Sammis, C.G., 1996. Development of strike-slip faults: shear experiments in granular materials and clay using a new technique. J. Struct. Geol. 18, 1061–1077. https://doi.org/10.1016/0191-8141(96)00012-0

Angster, S., Wesnousky, S., Figueiredo, P., Owen, L.A., Hammer, S., 2019. Late Quaternary slip rates for faults of the Central Walker Lane: Spatiotemporal strain release in a strike-slip fault system. Geosphere 57.

Angster, S., Wesnousky, S., Huang, W., Kent, G., Nakata, T., Goto, H., 2016. Application of UAV Photography to Refining the Slip Rate on the Pyramid Lake Fault Zone, Nevada. Bull. Seismol. Soc. Am. 106, 785–798. https://doi.org/10.1785/0120150144

Atmaoui, N., Kukowski, N., Stöckhert, B., König, D., 2006. Initiation and development of pull-apart basins with Riedel shear mechanism: insights from scaled clay experiments. Int. J. Earth Sci. 95, 225–238. https://doi.org/10.1007/s00531-005-0030-1

Aydin, A., Nur, A., 1982. Evolution of pull-apart basins and their scale independence. Tectonics 1, 91–105. https://doi.org/10.1029/TC001i001p00091

Balco, G., Stone, J.O., Lifton, N.A., Dunai, T.J., 2008. A complete and easily accessible means of calculating surface exposure ages or erosion rates from 10Be and 26Al measurements. Quat. Geochronol. 3, 174–195. https://doi.org/10.1016/j.quageo.2007.12.001

Beanland, S., Clark, M.M., 1994. The Owens Valley Fault Zone, Eastern California, and Surface Faulting Associated with the 1872 Earthquake (U.S. Geological Survey Bulletin No. 1982). U.S. Geological Survey.

Bell, J.W., Caskey, S.J., Ramelli, A.R., Guerrieri, L., 2004. Pattern and rates of faulting in the central Nevada seismic belt, and paleoseismic evidence for prior beltlike behavior. Bull. Seismol. Soc. Am. 94, 1229–1254.

Bell, J.W., dePolo, C.M., Ramelli, A.R., Sarna-Wojcicki, A.M., Meyer, C.E., 1999. Surface faulting and paleoseismic history of the 1932 Cedar Mountain earthquake area, west-central Nevada, and implications for modern tectonics of the Walker Lane. Geol. Soc. Am. Bull. 111, 791–807. https://doi.org/10.1130/0016-7606(1999)111<0791:SFAPHO>2.3.CO;2

Bennett, R.A., Wernicke, B.P., Niemi, N.A., Friedrich, A.M., Davis, J.L., 2003. Contemporary strain rates in the northern Basin and Range province from GPS data. Tectonics 22, 31 pp. https://doi.org/10.1029/2001TC001355

Borchers, B., Marrero, S., Balco, G., Caffee, M., Goehring, B., Lifton, N., Nishiizumi, K., Phillips, F., Schaefer, J., Stone, J., 2016. Geological calibration of spallation production rates in the CRONUS-Earth project. Quat. Geochronol. 31, 188–198. https://doi.org/10.1016/j.quageo.2015.01.009

Bormann, J.M., Hammond, W.C., Kreemer, C., Blewitt, G., 2016. Accommodation of missing shear strain in the Central Walker Lane, western North America: Constraints from dense GPS measurements. Earth Planet. Sci. Lett. 440, 169–177. https://doi.org/10.1016/j.epsl.2016.01.015

Bormann, J.M., Surpless, B.E., Caffee, M.W., Wesnousky, S.G., 2012. Holocene Earthquakes and Late Pleistocene Slip-Rate Estimates on the Wassuk Range Fault Zone, Nevada. Bull. Seismol. Soc. Am. 102, 1884–1891. https://doi.org/10.1785/0120110287

Briggs, R.W., 2005. Late Pleistocene and Holocene Paleoearthquake Activity of the Olinghouse Fault Zone, Nevada. Bull. Seismol. Soc. Am. 95, 1301–1313. https://doi.org/10.1785/0120040129

Briggs, R.W., 2004. Late Pleistocene fault slip rate, earthquake recurrence, and recency of slip along the Pyramid Lake fault zone, northern Walker Lane, United States. J. Geophys. Res. 109. https://doi.org/10.1029/2003JB002717

Calzolari, G., Rossetti, F., Seta, M.D., Nozaem, R., Olivetti, V., Balestrieri, M.L., Cosentino, D., Faccenna, C., Stuart, F.M., Vignaroli, G., 2016. Spatio-temporal evolution of intraplate strike-slip faulting: The Neogene–Quaternary Kuh-e-Faghan Fault, central Iran. GSA Bull. 128, 374–396. https://doi.org/10.1130/B31266.1

Carlson, C., 2017. Kinematics and Transfer Mechanisms of Strain Accommodation at the Transition between the Northern and Central Walker Lane, Western Nevada (Doctoral Dissertation). University of Nevada, Reno, Reno, NV.

Cashman, P.H., Fontaine, S.A., 2000. Strain partitioning in the northern Walker Lane, western Nevada and northeastern California. Tectonophysics 326, 111–130.

dePolo, C.M., Sawyer, T., 2005. Paleoseismic studies along the Eastern Carson Valley fault system (Final Technical Report), U.S. Geological Survey National Hazards Reduction Program.

Dixon, T.H., Miller, M., Farina, F., Wang, H., Johnson, D., 2000. Present-day motion of the Sierra Nevada block and some tectonic implications for the Basin and Range province, North American Cordillera. Tectonics 19, 1–24.

Dong, S., Ucarkus, G., Wesnousky, S.G., Maloney, J., Kent, G., Driscoll, N., Baskin, R., 2014. Strike-slip faulting along the Wassuk Range of the northern Walker Lane, Nevada. Geosphere 10, 40–48.

Dyksterhuis, S., Müller, R.D., 2008. Cause and evolution of intraplate orogeny in Australia. Geology 36, 495–498. https://doi.org/10.1130/G24536A.1

Faulds, J.E., Bouchot, V., Moeck, I., Oguz, K., 2009. Structural Controls on Geothermal Systems in Western Turkey: A Preliminary Report 33, 8.

Faulds, J.E., Henry, C.D., 2008. Tectonic influences on the spatial and temporal evolution of the Walker Lane: An incipient transform fault along the evolving Pacific – North American plate boundary 34.

Faulds, J.E., Henry, C.D., Hinz, N.H., 2005. Kinematics of the northern Walker Lane: An incipient transform fault along the Pacific–North American plate boundary. Geology 33, 505–508.

Frankel, K.L., Dolan, J.F., Finkel, R.C., Owen, L.A., Hoeft, J.S., 2007. Spatial variations in slip rate along the Death Valley-Fish Lake Valley fault system determined from LiDAR topographic data and cosmogenic 10Be geochronology. Geophys. Res. Lett. 34. https://doi.org/10.1029/2007GL030549

Frankel, K.L., Dolan, J.F., Owen, L.A., Ganev, P., Finkel, R.C., 2011. Spatial and temporal constancy of seismic strain release along an evolving segment of the Pacific–North America plate boundary. Earth Planet. Sci. Lett. 304, 565–576. https://doi.org/10.1016/j.epsl.2011.02.034

Ganev, P.N., Dolan, J.F., Frankel, K.L., Finkel, R.C., 2010. Rates of extension along the Fish Lake Valley fault and transtensional deformation in the Eastern California shear zone–Walker Lane belt. Lithosphere 2, 33–49. https://doi.org/10.1130/L51.1

Gilbert, C.M., Reynolds, M.W., 1973. Character and Chronology of Basin Development, Western Margin of the Basin and Range Province. Geol. Soc. Am. Bull. 84, 2489. https://doi.org/10.1130/0016-7606(1973)84<2489:CACOBD>2.0.CO;2

Gold, R., dePolo, C., Briggs, R., Crone, A., Gosse, J., 2013. Late Quaternary Slip-Rate Variations along the Warm Springs Valley Fault System, Northern Walker Lane, California–Nevada Border. Bull. Seismol. Soc. Am. 103, 542–558. https://doi.org/10.1785/0120120020

Gold, R.D., Briggs, R.W., Crone, A.J., DuRoss, C.B., 2017. Refining fault slip rates using multiple displaced terrace risers—An example from the Honey Lake fault, NE California, USA. Earth Planet. Sci. Lett. 477, 134–146. https://doi.org/10.1016/j.epsl.2017.08.021

Gold, R.D., Briggs, R.W., Personius, S.F., Crone, A.J., Mahan, S.A., Angster, S.J., 2014. Latest Quaternary paleoseismology and evidence of distributed dextral shear along the Mohawk Valley fault zone, northern Walker Lane, California: Paleoseismology Mohawk Valley fault zone. J. Geophys. Res. Solid Earth 119, 5014–5032. https://doi.org/10.1002/2014JB010987

Gold, R.D., Reitman, N.G., Briggs, R.W., Barnhart, W.D., Hayes, G.P., Wilson, E., 2015. On- and off-fault deformation associated with the September 2013 Mw 7.7 Balochistan earthquake: Implications for geologic slip rate measurements. Tectonophysics. https://doi.org/10.1016/j.tecto.2015.08.019

Gosse, J.C., Phillips, F.M., 2001. Terrestrial in situ cosmogenic nuclides: theory and application. Quat. Sci. Rev. 20, 1475–1560.

Gourmelen, N., Dixon, T.H., Amelung, F., Schmalzle, G., 2011. Acceleration and evolution of faults: An example from the Hunter Mountain–Panamint Valley fault zone, Eastern California. Earth Planet. Sci. Lett. 301, 337–344. https://doi.org/10.1016/j.epsl.2010.11.016

Guest, B., Niemi, N., Wernicke, B., 2007. Stateline fault system: A new component of the Miocene-Quaternary Eastern California shear zone. GSA Bull. 119, 1337–1347. https://doi.org/10.1130/0016-7606(2007)119[1337:SFSANC]2.0.CO;2

Haddon, E.K., Amos, C.B., Zielke, O., Jayko, A.S., Bürgmann, R., 2016. Surface slip during large Owens Valley earthquakes. Geochem. Geophys. Geosystems 17, 2239–2269. https://doi.org/10.1002/2015GC006033

Hamling, I.J., Hreinsdóttir, S., Clark, K., Elliott, J., Liang, C., Fielding, E., Litchfield, N., Villamor, P., Wallace, L., Wright, T.J., D’Anastasio, E., Bannister, S., Burbidge, D., Denys, P., Gentle, P., Howarth, J., Mueller, C., Palmer, N., Pearson, C., Power, W., Barnes, P., Barrell, D.J.A., Dissen, R.V., Langridge, R., Little, T., Nicol, A., Pettinga, J., Rowland, J., Stirling, M., 2017. Complex multifault rupture during the 2016 Mw 7.8 Kaikōura earthquake, New Zealand. Science 356, eaam7194. https://doi.org/10.1126/science.aam7194

Hammond, W.C., Blewitt, G., Kreemer, C., 2011. Block modeling of crustal deformation of the northern Walker Lane and Basin and Range from GPS velocities. J. Geophys. Res. 116. https://doi.org/10.1029/2010JB007817

Hammond, W.C., Thatcher, W., 2007. Crustal deformation across the Sierra Nevada, northern Walker Lane, Basin and Range transition, western United States measured with GPS, 2000–2004. J. Geophys. Res. 112. https://doi.org/10.1029/2006JB004625

Hammond, W.C., Thatcher, W., 2005. Northwest Basin and Range tectonic deformation observed with the Global Positioning System, 1999–2003. J. Geophys. Res. 110. https://doi.org/10.1029/2005JB003678

Hanks, T.C., Kanamori, H., 1979. A moment magnitude scale. J. Geophys. Res. Solid Earth 84, 2348–2350. https://doi.org/10.1029/JB084iB05p02348

Hatem, A.E., Cooke, M.L., Toeneboehn, K., 2017. Strain localization and evolving kinematic efficiency of initiating strike-slip faults within wet kaolin experiments. J. Struct. Geol. 101, 96–108. https://doi.org/10.1016/j.jsg.2017.06.011

Hecker, S., Dawson, T.E., Schwartz, D.P., 2010. Normal-Faulting Slip Maxima and Stress-Drop Variability: A Geological PerspectiveNormal-Faulting Slip Maxima and Stress-Drop Variability: A Geological Perspective. Bull. Seismol. Soc. Am. 100, 3130–3147. https://doi.org/10.1785/0120090356

Herbert, J.W., Cooke, M.L., Oskin, M., Difo, O., 2014. How much can off-fault deformation contribute to the slip rate discrepancy within the eastern California shear zone? Geology 42, 71–75. https://doi.org/10.1130/g34738.1

Hidy, A.J., Gosse, J.C., Pederson, J.L., Mattern, J.P., Finkel, R.C., 2010. A geologically constrained Monte Carlo approach to modeling exposure ages from profiles of cosmogenic nuclides: An example from Lees Ferry, Arizona. Geochem. Geophys. Geosystems 11. https://doi.org/10.1029/2010GC003084

Hunter, L.E., Howle, J.F., Rose, R.S., Bawden, G.W., 2011. LiDAR-Assisted Identification of an Active Fault near Truckee, California. Bull. Seismol. Soc. Am. 101, 1162–1181. https://doi.org/10.1785/0120090261

Kaneda, H., Okada, A., 2008. Long-Term Seismic Behavior of a Fault Involved in a Multiple-Fault Rupture: Insights from Tectonic Geomorphology along the Neodani Fault, Central Japan. Bull. Seismol. Soc. Am. 98, 2170–2190. https://doi.org/10.1785/0120070204

Kent, G.M., Babcock, J.M., Driscoll, N.W., Harding, A.J., Dingler, J.A., Seitz, G.G., Gardner, J.V., Mayer, L.A., Goldman, C.R., Heyvaert, A.C., Richards, R.C., Karlin, R., Morgan, C.W., Gayes, P.T., Owen, L.A., 2005. 60 k.y. record of extension across the western boundary of the Basin and Range province: Estimate of slip rates from offset shoreline terraces and a catastrophic slide beneath Lake Tahoe. Geology 33, 365–368. https://doi.org/10.1130/G21230.1

Kirby, E., Anandakrishnan, S., Phillips, F., Marrero, S., 2008. Late Pleistocene slip rate along the Owens Valley fault, eastern California. Geophys. Res. Lett. 35. https://doi.org/10.1029/2007GL031970

Kirby, E., Burbank, D.W., Reheis, M., Phillips, F., 2006. Temporal variations in slip rate of the White Mountain Fault Zone, Eastern California. Earth Planet. Sci. Lett. 248, 168–185. https://doi.org/10.1016/j.epsl.2006.05.026

Koehler, R.D., Wesnousky, S.G., 2011. Late Pleistocene regional extension rate derived from earthquake geology of late Quaternary faults across the Great Basin, Nevada, between 38.5° N and 40° N latitude. Geol. Soc. Am. Bull. 123, 631–650.

Kohl, C.P., Nishiizumi, K., 1992. Chemical isolation of quartz for measurement of in-situ-produced cosmogenic nuclides. Geochim. Cosmochim. Acta 56, 3583–3587.

Lal, D., 1991. Cosmic ray labeling of erosion surfaces: in situ nuclide production rates and erosion models. Earth Planet. Sci. Lett. 104, 424–439.

Lee, J., Spencer, J., Owen, L., 2001. Holocene slip rates along the Owens Valley fault, California: Implications for the recent evolution of the Eastern California Shear Zone. Geology 29, 819–822. https://doi.org/10.1130/0091-7613(2001)029<0819:HSRATO>2.0.CO;2

Li, X., Huang, W., Pierce, I.K.D., Angster, S.J., Wesnousky, S.G., 2017. Characterizing the Quaternary expression of active faulting along the Olinghouse, Carson, and Wabuska lineaments of the Walker Lane. Geosphere 13, 2119–2136. https://doi.org/10.1130/GES01483.1

Lifton, N., 2016. Implications of two Holocene time-dependent geomagnetic models for cosmogenic nuclide production rate scaling. Earth Planet. Sci. Lett. 433, 257–268. https://doi.org/10.1016/j.epsl.2015.11.006

Link, M.H., Roberts, M.T., Newton, M.S., 1985. Walker Lake Basin, Nevada: An Example of Late Tertiary (?) to Recent Sedimentation in a Basin Adjacent to an Active Strike-Slip Fault, in: Strike-Slip Deformation, Basin Formation, and Sedimentation. Society for Sedimentary Geology.

Maloney, J.M., Noble, P.J., Driscoll, N.W., Kent, G.M., Smith, S.B., Schmauder, G.C., Babcock, J.M., Baskin, R.L., Karlin, R., Kell, A.M., Seitz, G.G., Zimmerman, S., Kleppe, J.A., 2013. Paleoseismic history of the Fallen Leaf segment of the West Tahoe-Dollar Point fault reconstructed from slide deposits in the Lake Tahoe Basin, California-Nevada. Geosphere 9, 1065–1090. https://doi.org/10.1130/GES00877.1

Mann, P., 2007. Global catalogue, classification and tectonic origins of restraining- and releasing bends on active and ancient strike-slip fault systems. Geol. Soc. Lond. Spec. Publ. 290, 13–142. https://doi.org/10.1144/SP290.2

Martin, L.C.P., Blard, P.-H., Balco, G., Lavé, J., Delunel, R., Lifton, N., Laurent, V., 2017. The CREp program and the ICE-D production rate calibration database: A fully parameterizable and updated online tool to compute cosmic-ray exposure ages. Quat. Geochronol. 38, 25–49. https://doi.org/10.1016/j.quageo.2016.11.006

Matenco, L., Bertotti, G., Leever, K., Cloetingh, S., Schmid, S.M., Tărăpoancă, M., Dinu, C., 2007. Large-scale deformation in a locked collisional boundary: Interplay between subsidence and uplift, intraplate stress, and inherited lithospheric structure in the late stage of the SE Carpathians evolution. Tectonics 26. https://doi.org/10.1029/2006TC001951

Molnar, P., 1988. Continental tectonics in the aftermath of plate tectonics. Nature 335, 131. https://doi.org/10.1038/335131a0

Myers, W.B., Hamilton, W., 1964. The Hebgen Lake, Montana, earthquake of August 17, 1959 (No. 435– I), Geological Survey Professional Paper.

Nishiizumi, K., Winterer, E.L., Kohl, C.P., Klein, J., Middleton, R., Lal, D., Arnold, J.R., 1989. Cosmic ray production rates of 10Be and 26Al in quartz from glacially polished rocks. J. Geophys. Res. Solid Earth 94, 17907–17915. https://doi.org/10.1029/JB094iB12p17907

Oskin, M.E., Arrowsmith, J.R., Corona, A.H., Elliott, A.J., Fletcher, J.M., Fielding, E.J., Gold, P.O., Garcia, J.J.G., Hudnut, K.W., Liu-Zeng, J., Teran, O.J., 2012. Near-Field Deformation from the El Mayor–Cucapah Earthquake Revealed by Differential LIDAR. Science 335, 702–705. https://doi.org/10.1126/science.1213778

Personius, S.F., Briggs, R.W., Maharrey, J.Z., Angster, S.J., Mahan, S.A., 2017. A paleoseismic transect across the northwestern Basin and Range Province, northwestern Nevada and northeastern California, USA. Geosphere 13, 782–810. https://doi.org/10.1130/GES01380.1

Pierce, I.K.D., Wesnousky, S.G., Owen, L.A., 2017. Terrestrial cosmogenic surface exposure dating of moraines at Lake Tahoe in the Sierra Nevada of California and slip rate estimate for the West Tahoe Fault. Geomorphology 298, 63–71. https://doi.org/10.1016/j.geomorph.2017.09.030

Raimondo, T., Hand, M., Collins, W.J., 2014. Compressional intracontinental orogens: Ancient and modern perspectives. Earth-Sci. Rev. 130, 128–153. https://doi.org/10.1016/j.earscirev.2013.11.009

Ramelli, A.R., Bell, J.W., dePolo, C.M., Yount, J.C., 1999. Large-magnitude, late Holocene earthquakes on the Genoa fault, west-central Nevada and eastern California. Bull. Seismol. Soc. Am. 89, 1458–1472.

Redwine, J., Wakabayashi, J., Sawyer, T., Bormann, J.M., Kemp, C., Humphrey, J., Unruh, J., Briggs, R.W., Adams, K.D., Ramelli, A.R., Gold, R.D., Burke, R.M., 2015. The 2015 Annual Pacific Cell Friends of the Pleistocene field trip. From Mohawk Valley to Caribou Junction Middle and North Forks of the Feather River, northeastern California (Field Trip Guide).

Reheis, M., 1999. Extent of Pleistocene Lakes in the Western Great Basin. Miscellaneous Field Studies.

Rittase, W.M., Kirby, E., McDonald, E., Walker, J.D., Gosse, J., Spencer, J.Q.G., Herrs, A.J., 2014. Temporal variations in Holocene slip rate along the central Garlock fault, Pilot Knob Valley, California. Lithosphere 6, 48–58. https://doi.org/10.1130/L286.1

Rood, D.H., Burbank, D.W., Finkel, R.C., 2011. Spatiotemporal patterns of fault slip rates across the Central Sierra Nevada frontal fault zone. Earth Planet. Sci. Lett. 301, 457–468. https://doi.org/10.1016/j.epsl.2010.11.006

Sarmiento, A.C., Wesnousky, S.G., Bormann, J.M., 2011. Paleoseismic Trenches across the Sierra Nevada and Carson Range Fronts in Antelope Valley, California, and Reno, Nevada. Bull. Seismol. Soc. Am. 101, 2542–2549. https://doi.org/10.1785/0120100176

Schreurs, G., 2003. Fault development and interaction in distributed strike-slip shear zones: an experimental approach. Geol. Soc. Lond. Spec. Publ. 210, 35–52. https://doi.org/10.1144/GSL.SP.2003.210.01.03

Seitz, G.G., Kent, G., 2014. Closing the Gap between on and Offshore Paleoseismic Records in the Lake Tahoe Basin (Final Technical Report), U.S. Geological Survey National Hazards Reduction Program.

Stauffer, H., 2003. Timing of the Last Highstand of Pluvial Lake Wellington, Smith Valley, Nevada (Master's Thesis). San Jose State University.

Stirling, M.W., Wesnousky, S.G., Shimazaki, K., 1996. Fault trace complexity, cumulative slip, and the shape of the magnitude-frequency distribution for strike-slip faults: a global survey. Geophys. J. Int. 124, 833–868. https://doi.org/10.1111/j.1365-246X.1996.tb05641.x

Stockli, D.F., Dumitru, T.A., McWilliams, M.O., Farley, K.A., 2003. Cenozoic tectonic evolution of the White Mountains, California and Nevada. Geol. Soc. Am. Bull. 115, 788–816.

Stone, J.O., 2000. Air pressure and cosmogenic isotope production. J. Geophys. Res. 105, 23,753-23,759.

Surpless, B., Kroeger, G., 2015. The unusual temporal and spatial slip history of the Wassuk Range normal fault, western Nevada (USA): Implications for seismic hazard and Walker Lane deformation. Geol. Soc. Am. Bull. 127, 737–758. https://doi.org/10.1130/B31159.1

Surpless, B.E., Stockli, D.F., Dumitru, T.A., Miller, E.L., 2002. Two-phase westward encroachment of Basin and Range extension into the northern Sierra Nevada. Tectonics 21, 2-1-2–10. https://doi.org/10.1029/2000tc001257

Tapponnier, P., Armijo, R., Manighetti, I., Courtillot, V., 1990. Bookshelf faulting and horizontal block rotations between overlapping rifts in southern Afar. Geophys. Res. Lett. 17, 1–4. https://doi.org/10.1029/GL017i001p00001

Thatcher, W., Foulger, G.R., Julian, B.R., Svarc, J., Quilty, E., Bawden, G.W., 1999. Present-Day Deformation Across the Basin and Range Province, Western United States. Science 283, 1714–1717.

Unruh, J., Humphrey, J., Barron, A., 2003. Transtensional model for the Sierra Nevada frontal fault system, eastern California. Geology 31, 327–330.

Uppala, S.M., KAllberg, P.W., Simmons, A.J., Andrae, U., Bechtold, V.D.C., Fiorino, M., Gibson, J.K., Haseler, J., Hernandez, A., Kelly, G.A., Li, X., Onogi, K., Saarinen, S., Sokka, N., Allan, R.P., Andersson, E., Arpe, K., Balmaseda, M.A., Beljaars, A.C.M., Berg, L.V.D., Bidlot, J., Bormann, N., Caires, S., Chevallier, F., Dethof, A., Dragosavac, M., Fisher, M., Fuentes, M., Hagemann, S., H?lm, E., Hoskins, B.J., Isaksen, L., Janssen, P.A.E.M., Jenne, R., Mcnally, A.P., Mahfouf, J.-F., Morcrette, J.-J., Rayner, N.A., Saunders, R.W., Simon, P., Sterl, A., Trenberth, K.E., Untch, A., Vasiljevic, D., Viterbo, P., Woollen, J., 2005. The ERA-40 re-analysis. Q. J. R. Meteorol. Soc. 131, 2961–3012. https://doi.org/10.1256/qj.04.176

Wesnousky, S.G., 2008. Displacement and Geometrical Characteristics of Earthquake Surface Ruptures: Issues and Implications for Seismic-Hazard Analysis and the Process of Earthquake Rupture. Bull. Seismol. Soc. Am. 98, 1609–1632. https://doi.org/10.1785/0120070111

Wesnousky, S.G., 2005. Active faulting in the Walker Lane. Tectonics 24, 35 pp. https://doi.org/10.1029/2004TC001645

Wesnousky, S.G., 1988. Seismological and structural evolution of strike-slip faults. Nature 335, 340. https://doi.org/10.1038/335340a0

Wesnousky, S.G., Bormann, J.M., Kreemer, C., Hammond, W.C., Brune, J.N., 2012. Neotectonics, geodesy, and seismic hazard in the Northern Walker Lane of Western North America: Thirty kilometers of crustal shear and no strike-slip? Earth Planet. Sci. Lett. 329–330, 133–140. https://doi.org/10.1016/j.epsl.2012.02.018

Wesnousky, S.G., Caffee, M., 2011. Range-Bounding Normal Fault of Smith Valley, Nevada: Limits on Age of Last Surface-Rupture Earthquake and Late Pleistocene Rate of Displacement. Bull. Seismol. Soc. Am. 101, 1431–1437. https://doi.org/10.1785/0120100238

Wilcox, R.E., Harding, T.P., Seely, D.R., 1973. Basic wrench tectonics. AAPG Bull. 57, 74–96.

Wintle, A.G., Murray, A.S., 2006. A review of quartz optically stimulated luminescence characteristics and their relevance in single-aliquot regeneration dating protocols. Radiat. Meas. 41, 369–391. https://doi.org/10.1016/j.radmeas.2005.11.001

Xu, X., Ma, X., Deng, Q., 1993. Neotectonic activity along the Shanxi rift system, China. Tectonophysics 219, 305–325. https://doi.org/10.1016/0040-1951(93)90180-R

Zechar, J.D., Frankel, K.L., 2009. Incorporating and reporting uncertainties in fault slip rates. J. Geophys. Res. Solid Earth 114, B12407. https://doi.org/10.1029/2009JB006325

Zhao, B., Zhang, C., Wang, D., Huang, Y., Tan, K., Du, R., Liu, J., 2017. Contemporary kinematics of the Ordos block, North China and its adjacent rift systems constrained by dense GPS observations. J. Asian Earth Sci. 135, 257–267. https://doi.org/10.1016/j.jseaes.2016.12.045

Ziegler, P.A., van Wees, J.-D., Cloetingh, S., 1998. Mechanical controls on collision-related compressional intraplate deformation. Tectonophysics 300, 103–129. https://doi.org/10.1016/S0040-1951(98)00236-4

Zinke, R., Dolan, J.F., Dissen, R.V., Grenader, J.R., Rhodes, E.J., McGuire, C.P., Langridge, R.M., Nicol, A., Hatem, A.E., 2015. Evolution and progressive geomorphic manifestation of surface faulting: A comparison of the Wairau and Awatere faults, South Island, New Zealand. Geology 43, 1019–1022. https://doi.org/10.1130/G37065.1

Zuza, A.V., Yin, A., Lin, J., Sun, M., 2017. Spacing and strength of active continental strike-slip faults. Earth Planet. Sci. Lett. 457, 49–62. https://doi.org/10.1016/j.epsl.2016.09.041